

Diffraction and Low- Q^2 Physics Including Two-Photon Physics

Martin Erdmann

Universität Karlsruhe, Engesserstr. 7, D-76128 Karlsruhe

E-mail: Martin.Erdmann@desy.de

Abstract

Recent experimental results on the partonic structure of the photon and on the color singlet exchange in strong interaction processes are reviewed. At the LEP e^+e^- and HERA ep colliders, complementary and consistent measurements have been achieved on the quark-gluon structure of quasi-real and virtual photons. At the HERA ep and Tevatron $p\bar{p}$ colliders, the quark-gluon configuration of the diffractive exchange is consistently found to have a large gluon component. The rate of diffractive interactions observed by the HERA and Tevatron experiments, however, is largely different and challenges explanation.

Invited plenary talk at the XXIX International Conference on High Energy Physics, Vancouver, B.C. Canada (1998)

1 The Partonic Structure of the Photon

The motivation behind studying the structure of the photon results from the interest in understanding the formation of hadronic matter. Permitted by the Heisenberg uncertainty relation, the photon can fluctuate for some time into a quark–anti-quark state. This fluctuation can be disturbed, e.g., by an electron or proton probe which allows the density of quarks and gluons of the partonic state of the photon to be determined.

At the LEP e^+e^- and HERA ep colliders, photons are emitted by the leptons which gives access to the partonic structure of almost real photons [1] as well as highly virtual photons. The measurements to obtain information on the partonic state of the photons discussed here are

1. the photon structure function from deep inelastic electron–photon scattering (Fig. 1),
2. jet and particle cross sections (e.g. Fig. 2), and
3. the total photon–photon cross section.

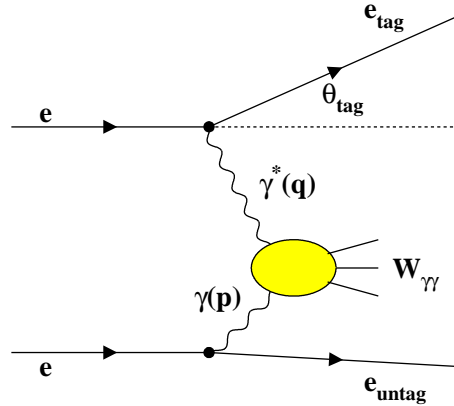


Figure 1: Feynman diagram of deep inelastic electron–photon scattering: the partonic structure of the quasi-real photon from the untagged lepton is probed by the virtual photon from the tagged electron.

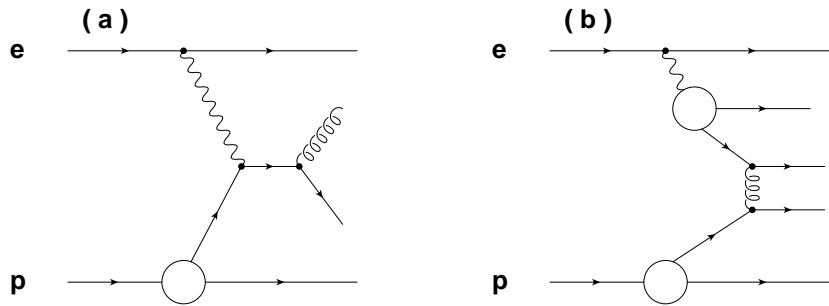


Figure 2: Examples of Feynman diagrams for photoproduction of jets in ep collisions in leading order QCD: a) direct photon–proton process, b) resolved photon–proton process.

1.1 Measurements Related to the Quark Distributions of Quasi-Real Photons

New F_2^γ structure function measurements have been performed in the interesting region of small parton momenta $x \sim 10^{-2}$ by the L3 collaboration [2]. F_2^γ is determined from the measurement of the double differential inclusive cross section

$$\frac{d^2\sigma}{dx dQ^2} = \frac{2\pi\alpha^2}{x Q^4} (1 + (1-y)^2) F_2^\gamma(x, Q^2), \quad (1)$$

where α is the electro-magnetic coupling constant, Q^2 denotes the virtuality of the probing photon and gives the resolution scale of the process, and y is the inelasticity $y = Q^2/(xs_{e\gamma})$. In Fig. 3, the x dependence of F_2^γ is shown in two bins of Q^2 .

A major challenge in this analysis is the determination of x : since the lepton that emitted the target photon remains undetected, the energy of the target has to be determined from the hadronic final state. Using a new improved reconstruction method for x , two results for F_2^γ are presented by the L3 collaboration using two different Monte Carlo generators for the correction of detector effects (Phojet [3], Twogam [4]). These two data sets demonstrate that over a large region in x the structure function result does not depend on the details of simulating the hadronic final state. Only below $x \sim 10^{-2}$ this limitation becomes sizable.

In the same figure, previous results of the OPAL collaboration are shown [5]. Within the errors, good agreement is observed between the two experiments. Also shown are different parameterizations of the quark density in the photon demonstrating that the data give new information on the quark distributions at low x (LAC [6], GRV [7], SaS [8]). Scaling violations caused by gluon emission off the quark before the scattering process occurs results in a rise of F_2^γ below a small value of x . The data are not yet precise enough to confirm or reject such a rise at $x \sim 10^{-2}$.

In the momentum region around $x \sim 0.5$, where the quark and the anti-quark each carry half of the photon energy, results on the structure function F_2^γ exist from many experiments. A compilation of these measurements is shown in Fig. 4 as a function of the resolution scale Q^2 [9]. The data are compatible with an increasing quark density in the photon as Q^2 increases. This Q^2 dependence is very different from that of hadronic structure functions at large x and is expected by perturbative QCD (Fig. 5 and discussion in Section 2.2): the splitting of the photon into a quark-anti-quark pair gives rise to the probability $f_{q/\gamma}$ of finding a quark in the photon to increase as

$$f_{q/\gamma} \sim \ln \frac{Q^2}{\Lambda_{QCD}^2} \quad (2)$$

in leading order.

In the same figure an effective parton distribution $x\tilde{f}_\gamma$ of the photon is shown which has been extracted from di-jet measurements in photon-proton collisions by the H1 collaboration [10]. This effective parton distribution combines the quark and the gluon densities of the photon with a weight of color factors [11]:

$$x\tilde{f}_\gamma = x (f_{q/\gamma} + \frac{9}{4} f_{g/\gamma}). \quad (3)$$

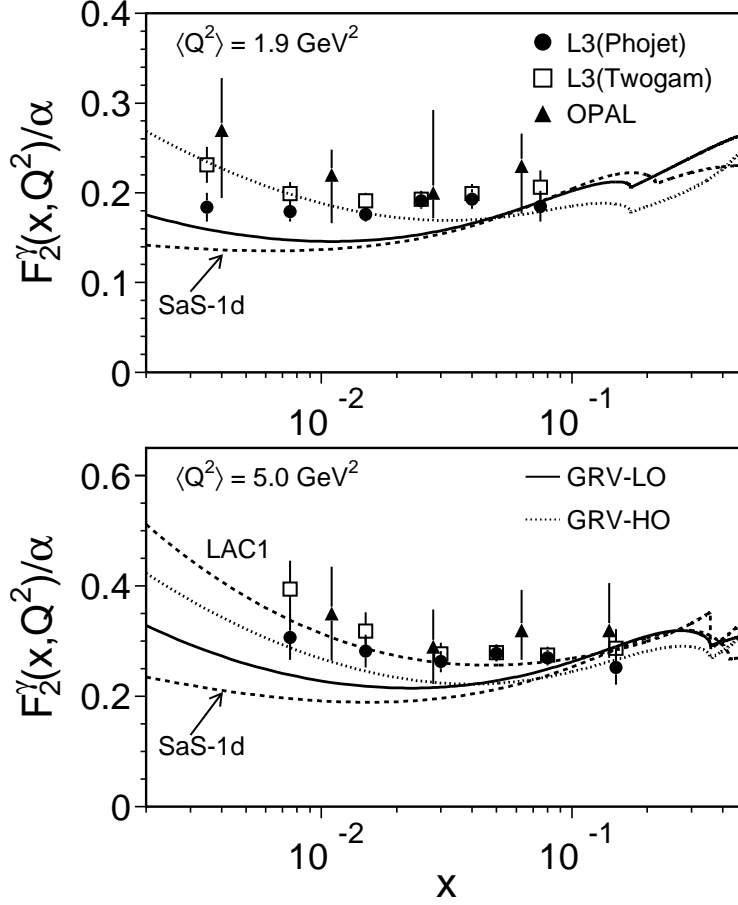


Figure 3: The photon structure function F_2^γ , measured in two-photon collision at LEP, is shown as a function of the parton fractional momentum x in two bins of the virtuality Q^2 of the probing photon. The squared symbols and the circles represent the measurements of the L3 experiment using two different Monte Carlo generators for correcting detector effects. For comparison, previous results of the OPAL experiment are shown (triangle symbols). The curves represent different parameterizations of the parton distributions in the photon.

The vertical scale for $x\tilde{f}_\gamma$ on the right side of Fig.4 has been adjusted relative to the F_2^γ scale, since in contrast to the F_2^γ measurements the jet processes are independent of the electric charges of the quarks. The relevant resolution scale is the transverse momentum p_t^2 of the scattered partons which is here taken to have the same resolution power as Q^2 . The results of the di-jet measurements are in good agreement with the F_2^γ data. The jet data probe the partons of the photon at large resolution scales and compete well in precision with the F_2^γ measurements.

The quark density close to the kinematic limit $x \sim 1$ is analysed in photoproduction of two jets. Here the contributions of the direct and resolved photon-proton processes need to be understood (Fig. 2). They differ in their matrix elements and therefore in the distribution of the parton scattering angle θ^* .

In Fig. 6, a new di-jet cross section measurement of the ZEUS collaboration is shown differentially in $|\cos \theta^*|$ for large di-jet masses and correspondingly large x [12]. Also shown are next-to-leading order QCD calculations [13] using two different parton parameterizations of

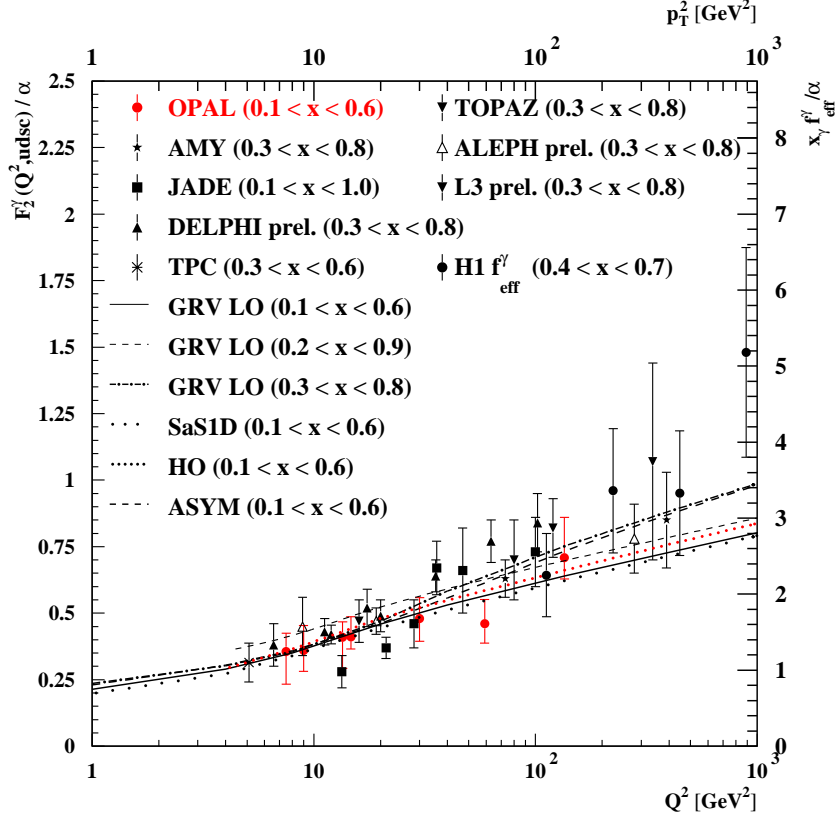


Figure 4: The structure function F_2 of the photon is shown as a function of the virtuality Q^2 of the probing photon for parton fractional momenta around $x \sim 0.5$. Measurements of the photon structure function F_2^γ from e^+e^- data are shown in comparison with an effective parton distribution extracted from photoproduction of di-jets in ep collisions (H1 data). The curves represent different parameterizations of the parton distributions of the photon.

the photon (GRV [7], GS [14]). The direct photon contribution (not shown in the figure) is not sufficient to describe the measured jet cross section either in shape or in the absolute normalization. Contributions of resolved photon processes are required to describe the data which are sufficiently precise to discriminate different parton parameterizations of the photon at large x .

1.2 Measurements Related to the Gluon Distribution of Quasi-Real Photons

New measurements of the inclusive charm production cross section at the large LEP beam energies are shown in Fig. 7 by the L3 collaboration [15]. The cross section has been determined using semi-leptonic charm decays in the electron and muon channels. In the same figure, next-to-leading order QCD calculations [16] using two different charm masses and the GRV parameterization [7] of the parton distributions in the photons are shown. The dominant contribution to the cross section results from gluon induced processes with an average gluon momentum as small as $\langle x \rangle \sim 0.03$ [17].

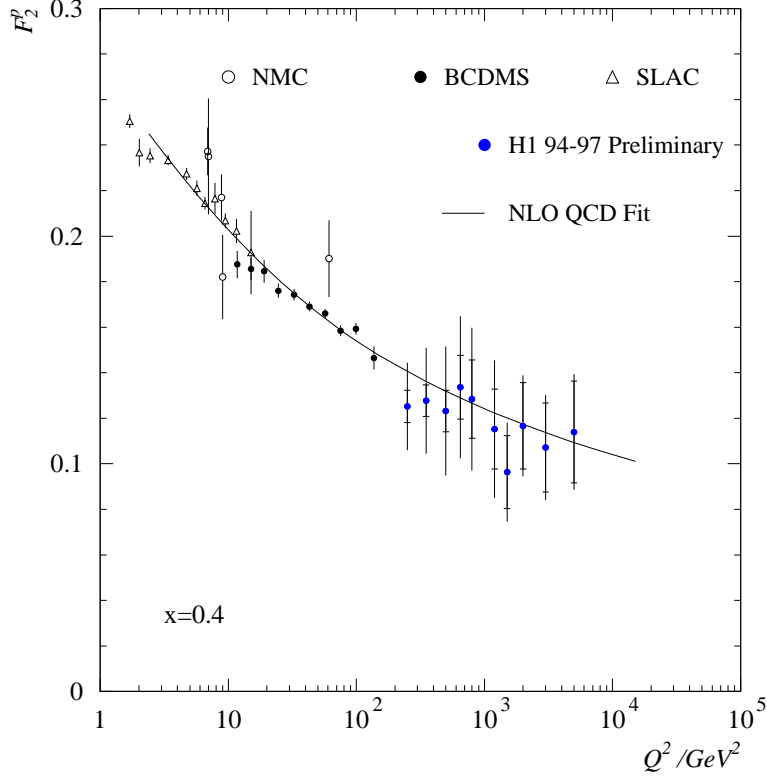


Figure 5: The structure function F_2 of the proton is shown as a function of the virtuality Q^2 of the probing photon for the parton fractional momentum $x = 0.4$ from fixed target data and preliminary H1 data.

Also di-jet data are used to access the low- x gluon distributions of the photon. In Fig. 8, a new measurement of the di-jet cross section is shown as a function of the parton momentum x by the H1 collaboration [18]. The histograms represent a leading-order QCD calculation [3] showing the contributions of the direct photon-proton interactions and quark and gluon induced processes using the GRV parton parameterizations for the photon and the proton.

Both the charm and di-jet measurements give compatible conclusions on the low- x gluon density of the photon and are precise to the level of 30%.

New information on the gluon distribution of the photon results from di-jet production in photon-photon collisions which has been measured by the OPAL collaboration [19]. In Fig. 9, the cross section is shown differentially in the transverse jet energy E_t^{jet} . At sufficiently large E_t^{jet} the measurement can well be described by a next-to-leading order QCD calculation [20] using the parton distribution function of GRV [7].

In Fig. 10, the di-jet cross sections are shown differentially in the jet rapidity $|\eta^{jet}|$. The data explore different regions of the parton fractional momentum $x > 0.8, x < 0.8$ with a precision of $\sim 20\%$. They are compared to leading order QCD calculations (Phojet [3], Pythia [21]) and discriminate different parameterizations of the gluon distributions of the photon (LAC [6], GRV [7], SaS [8]).

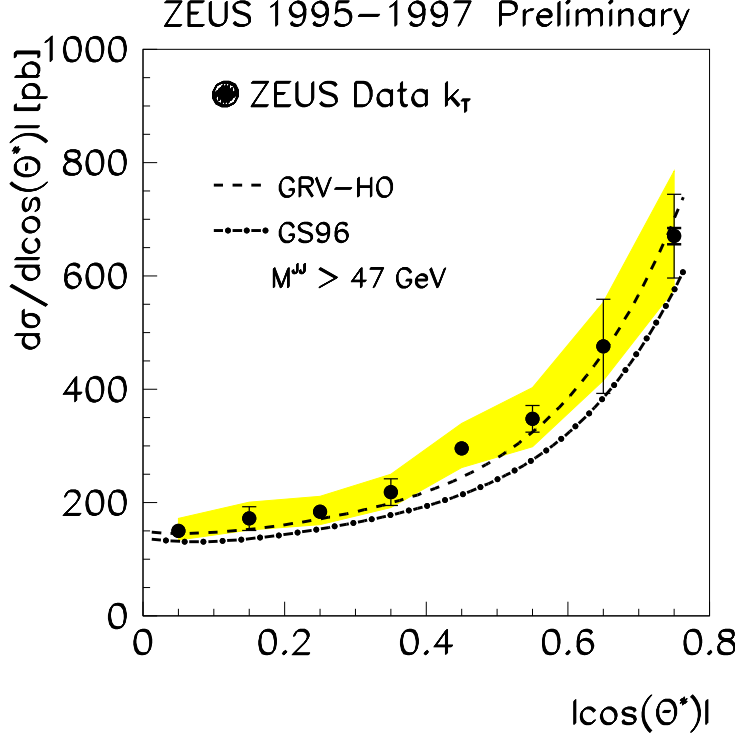


Figure 6: The di-jet cross section in ep collisions involving quasi-real photons is shown differentially in terms of the cosine of the parton scattering angle at large di-jet mass above 47 GeV from ZEUS data. The curves represent next-to-leading QCD calculations using different parton distributions of the photon.

1.3 Parton Distributions of Virtual Photons

The fluctuation of a virtual photon into a quark-anti-quark pair is suppressed by the photon virtuality Q^2 . In comparison with real photons one therefore expects a smaller probability of finding the virtual photon in a partonic state. Also, there is less time to develop from the $q\bar{q}$ pair a vector meson bound state such that the hadronic contributions to the virtual photon structure should be small.

In Fig. 11, the first triple-differential di-jet cross section is shown as a function of the photon virtuality Q^2 in two bins of the parton momentum x for a fixed resolution scale $(E_t^{jet})^2 = 50 \text{ GeV}^2$ [22]. The cross section measurement at $x \sim 1$ (Fig. 11b) is well described by a leading order QCD calculation using the direct photon-proton interaction processes only (dashed curve [23]). At $x \sim 0.5$ (Fig. 11a) the absolute cross section is found to be smaller compared to the measurement at $x \sim 1$ as expected from the short fluctuation time of the photon. Here the direct photon contributions are not sufficient to describe the data at small $Q^2 \sim 2 \text{ GeV}^2$: the di-jet process is able to resolve the partonic structure of the virtual photon. As Q^2 approaches the squared transverse energy of the jets of $(E_t^{jet})^2 = 50 \text{ GeV}^2$, the resolution power of the di-jet process becomes insufficient for detecting the fluctuations of the virtual photons.

In analogy to the real photon case, eq. (3), an effective parton distribution for virtual photons $x\tilde{f}_{\gamma^*} = x(f_{q/\gamma^*} + 9/4 f_{g/\gamma^*})$ has been extracted from the data and is shown in Fig. 12a in the

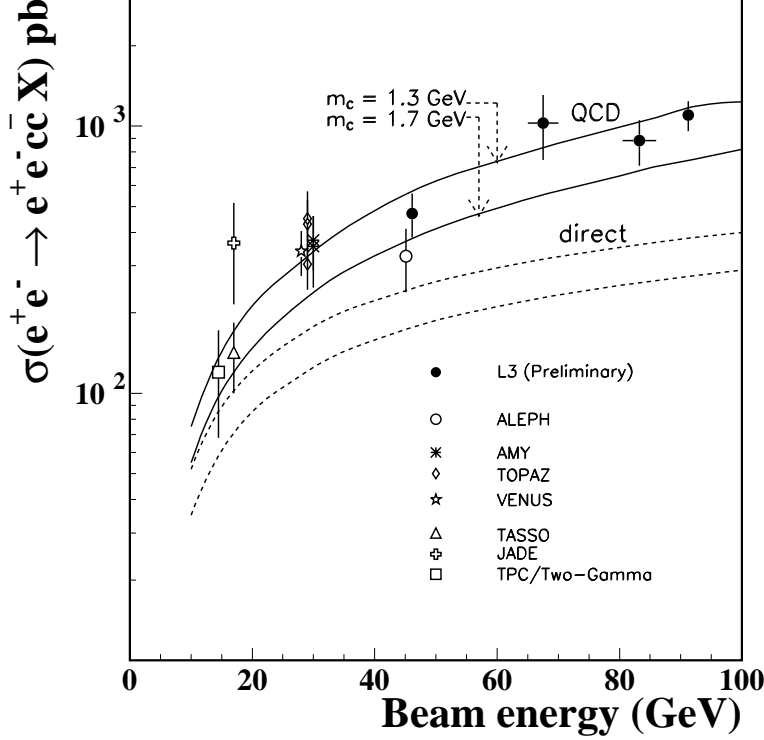


Figure 7: Measurements of the total charm production cross sections from two-photon collisions are shown as a function of the lepton beam energy (L3 experiment). The full curves represent next-to-leading QCD calculations using the GRV parton distribution functions of the photon and different values for the charm mass. The direct photon contribution is shown separately (dashed curves).

interval $0 \leq Q^2 \leq 80 \text{ GeV}^2$ for $x = 0.6$ and $(E_t^{jet})^2 = 85 \text{ GeV}^2$. The partonic structure of the virtual photon is only slowly suppressed with the photon virtuality Q^2 . Such a dependence is predicted by perturbative QCD: in the region of $\Lambda_{QCD}^2 < Q^2 < (E_t^{jet})^2$ the probability of finding a quark in the virtual photon decreases logarithmically as Q^2 approaches the jet resolution scale:

$$f_{q/\gamma^*} \sim \ln \frac{(E_t^{jet})^2}{Q^2}. \quad (4)$$

The formation of a hadronic bound state from the $q\bar{q}$ pair of the photon can be studied with the production of ρ mesons. In Fig. 12b, the Q^2 dependence of the ρ cross section is shown which exhibits a fast decrease proportional to $(Q^2 + M_\rho^2)^{-n}$ with $n = 2.24 \pm 0.09$ [24]. As expected from the short photon fluctuation time into a quark-anti-quark pair, the probability to develop a hadronic bound state from the quark-anti-quark pair is highly suppressed. At sufficiently large Q^2 , the partonic structure of the virtual photon can therefore be predicted by perturbative QCD. In Fig. 12a, the full curve represents a QCD inspired model of the effective parton distribution of the virtual photon (SaS1d [25]) which is in agreement with the measurement within the experimental errors.

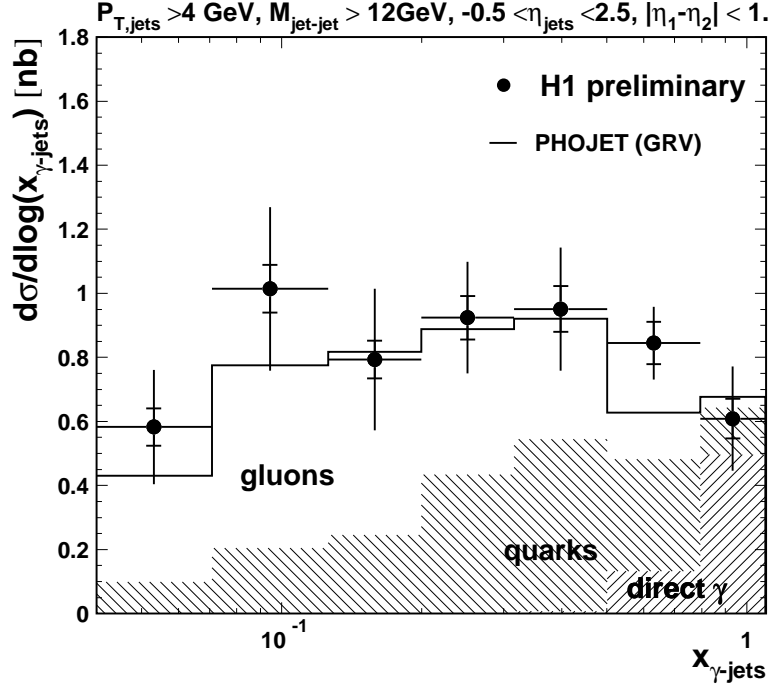


Figure 8: Photoproduction of di-jets in ep collisions is shown as a function of the parton fractional momentum x from H1 data. The cross section measurement is compared to a leading-order QCD calculation showing above the quark and direct photon contributions the gluon component of the photon at small x (the histograms are calculated using the GRV parameterizations of the partons in the photon).

1.4 Total Photon-Photon Cross Section

The total photon-photon cross section $\sigma_{\gamma\gamma}$ is dominated by soft scattering processes in which the photons develop a hadronic structure before the interaction occurs. A major challenge of this measurement is the understanding of the different contributions, the elastic, diffractive and non-diffractive processes. The visibility of the first two contributions in the detectors is small and requires reliable Monte Carlo generator calculations.

Progress has recently been made by the L3 experiment which succeeded in collecting a few hundred events of exclusive four pion production which contains contributions of elastic double- ρ production at center of mass energies below 10 GeV (Fig. 13) [26]. These data test the two generator calculations shown (Phojet [3], Pythia [21]).

A new measurement of the total photon-photon cross section is shown in Fig. 14 using the two different Monte Carlo generators (L3 collaboration [26, 27]). The data show a rise above $W \equiv \sqrt{s_{\gamma\gamma}} = 10$ GeV and are compatible within errors with the preliminary measurement of the OPAL collaboration [28]. This observed rise can be described by a power law $s_{\gamma\gamma}^\epsilon$ with $\epsilon = 0.158 \pm 0.006 \pm 0.028$ [26]. The rise has the tendency to be stronger than expected from soft Pomeron exchange which successfully describes all hadron-hadron and photon-proton total cross sections with $\epsilon = 0.095 \pm 0.002$ [29].

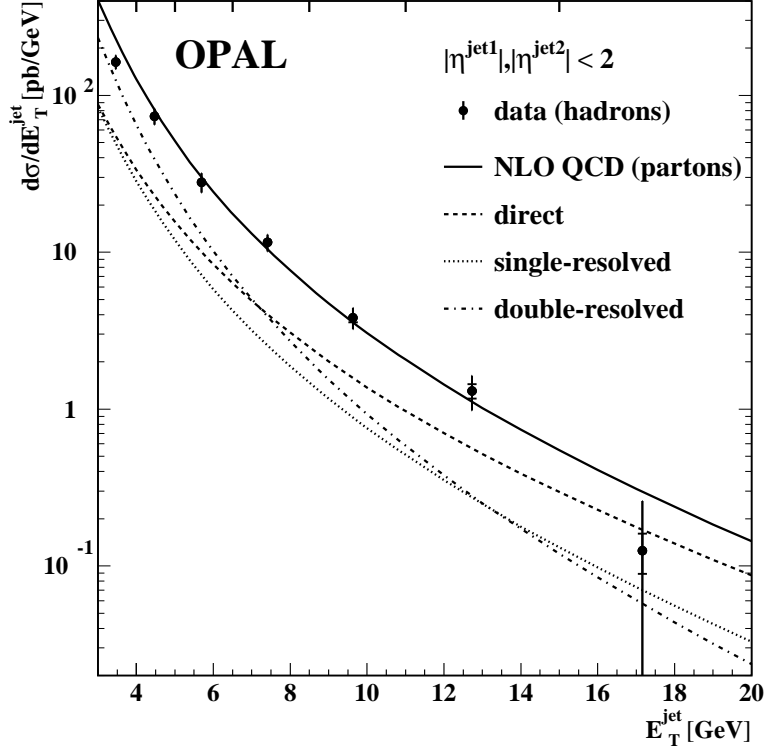


Figure 9: The di-jet cross sections from two-photon processes in e^+e^- collisions is shown as a function of the transverse jet energy from OPAL data. The curves represent next-to-leading QCD calculations of the different photon contributions using the GRV parton distribution functions of the photon. The labels refer to direct photon-photon interactions via quark exchange (direct), processes where one photon interacts directly with a parton of the other photon (single resolved) and processes which involve partons of both photons (double resolved).

1.5 Summary 1: Photon

Improved knowledge on the partonic structure of real photons results from

- new structure function F_2^γ measurements at low parton fractional momenta $x \sim 10^{-2}$,
- di-jet cross section measurements at x values down to $\sim 10^{-2}$ and high $x \rightarrow 1$ in photon-proton and photon-photon interactions, and
- charm production in photon-photon processes at low $x \sim 10^{-2}$.

For the first time the partonic structure of highly virtual photons $Q^2 > 1 \text{ GeV}^2$ has been investigated in ep collisions. The fluctuations of the virtual photon into a quark-anti-quark pair is only slowly suppressed with Q^2 and is compatible with a logarithmic decrease as predicted by perturbative QCD.

The understanding of the total photon-photon cross section has improved by the detection of elastic ρ production.

Overall, the results on the photon obtained in e^+e^- and ep collisions complement each other and are well compatible. The precision of the measurements remains a challenge for the next few years in order to be well prepared for the linear collider.

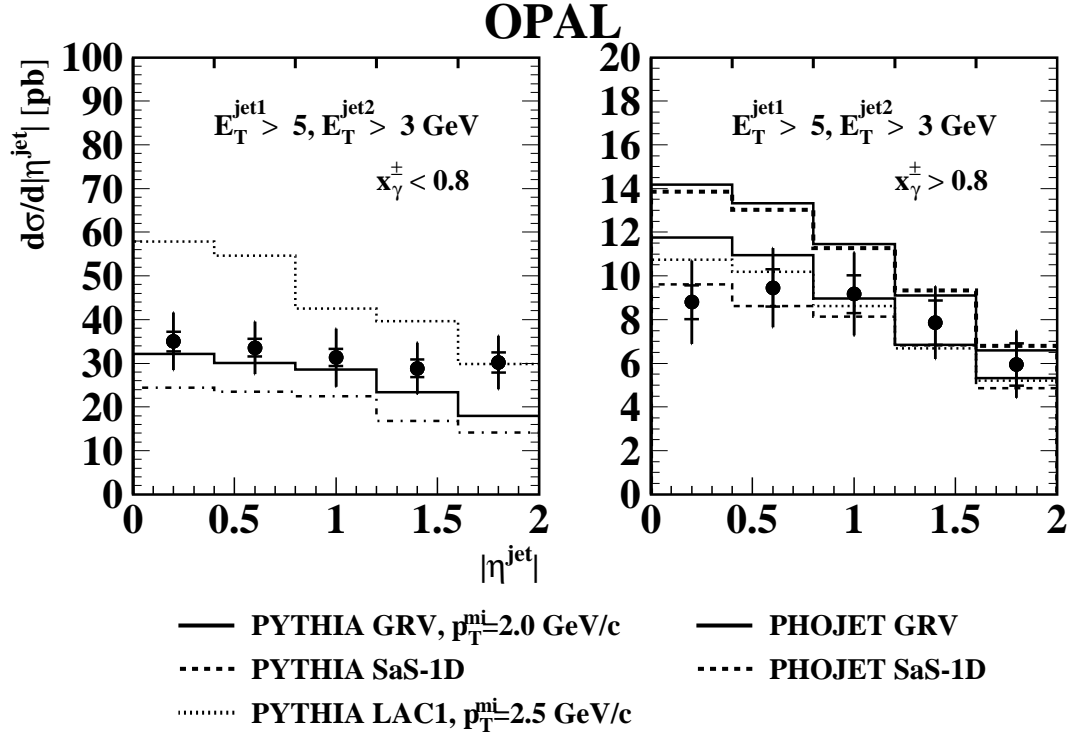


Figure 10: The di-jet cross sections from two-photon processes in e^+e^- collisions is shown differentially in terms of the jet pseudo-rapidity in two bins of the reconstructed parton fractional momentum x of the photon (OPAL experiment). The histograms represent leading order QCD calculations of two Monte Carlo generators using different parton distribution functions for the photon.

2 Colour Singlet Exchange

A sizable fraction of strong interaction processes includes the exchange of colour singlet objects. At the HERA ep and Tevatron $p\bar{p}$ colliders, these objects are emitted by the hadrons and may involve the exchange of quantum numbers (meson exchange) or may not (diffractive processes).

A handle on the type of the interaction process is given, e.g., by the observation of a fast baryon in the proton beam direction. Detection of energetic neutrons indicate that isospin-1 exchanges are present, in particular charged pion exchange. Protons are sensitive to both isoscalar and isovector exchanges.

Where the leading proton is close to the beam energy, diffractive scattering is expected to be dominant. Partonic scattering processes in such diffractive interactions give access to quark-gluon configurations that are colour neutral but different from the well known hadrons.

The following measurements to obtain information on colour singlet exchange are discussed here:

1. the ep structure function with a tagged baryon (Fig. 15),

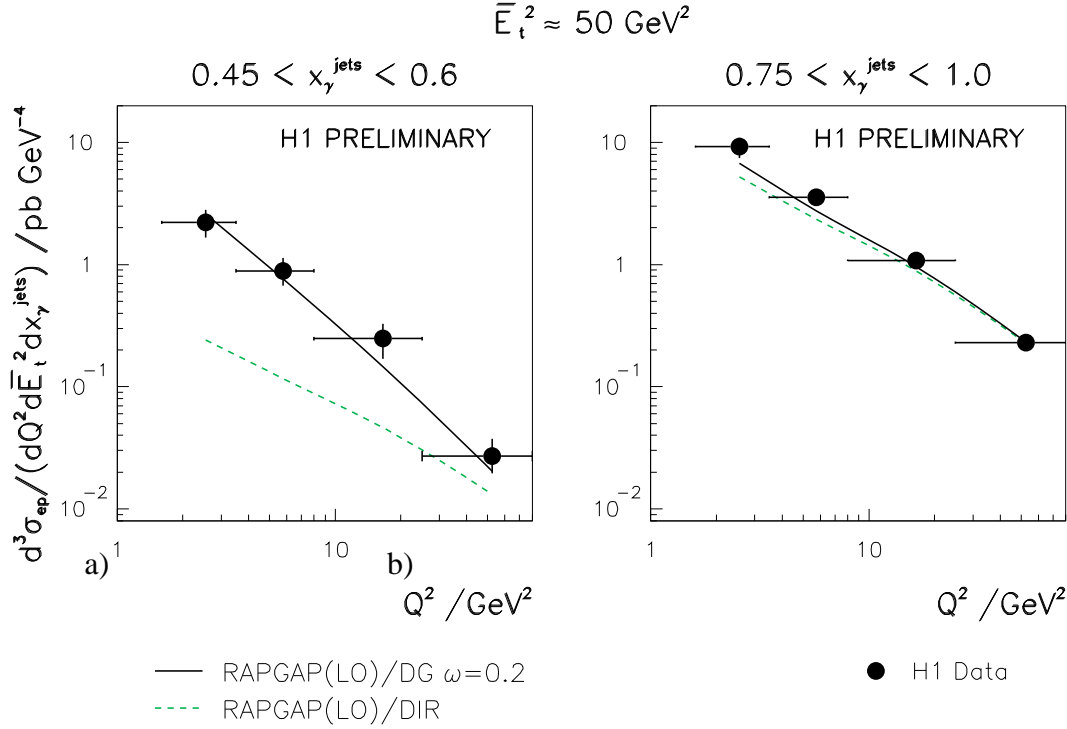


Figure 11: The triple differential di-jet cross section from ep collisions is shown as a function of the photon virtuality Q^2 for two bins of the fractional momentum x of the parton from the photon at fixed transverse jet energy E_t^{jet} (H1 experiment). The full curve is a leading order QCD calculation including the direct photon–proton interactions (dashed curve) and resolved photon processes, the latter reflecting the partonic structure of the virtual photon.

2. the ep structure function of diffractive exchange (Figs. 15 “ \mathbb{P} ” and 17),
3. di-jet and W-boson production in diffractive $\bar{p}p$ scattering (Fig. 22), and
4. vector meson production in ep interactions (Fig. 28).

2.1 Tagged Baryon Production in ep Collisions

The production of protons and neutrons is studied in both the H1 and ZEUS experiments. A hadron calorimeter detects neutrons scattered at zero angle with respect to the proton direction. A series of Roman pot stations between the beam magnets serves as a proton spectrometer.

In Fig. 16, new measurements of the structure function from ep collisions with a tagged baryon $F_2^{\text{LB}(3)}$ are shown as a function of the baryon fractional energy $z = E_{lb}/E_p$ for fixed photon virtuality $Q^2 = 4.4 \text{ GeV}^2$ and parton fractional momentum $x_{Bj} = 10^{-3}$ (H1 collaboration [30]). $F_2^{\text{LB}(3)}$ was determined from cross section measurements which were integrated over the baryon transverse momenta in the range $0 \leq p_t \leq 0.2 \text{ GeV}$:

$$\frac{d^3\sigma}{dx_{Bj}dQ^2dz} = \frac{2\pi\alpha^2}{x_{Bj}Q^4} (1 + (1-y)^2) F_2^{\text{LB}(3)}(x_{Bj}, Q^2, z). \quad (5)$$

Here α is the electro-magnetic coupling constant and y denotes the inelasticity $y = Q^2/(x_{Bj}s_{ep})$.

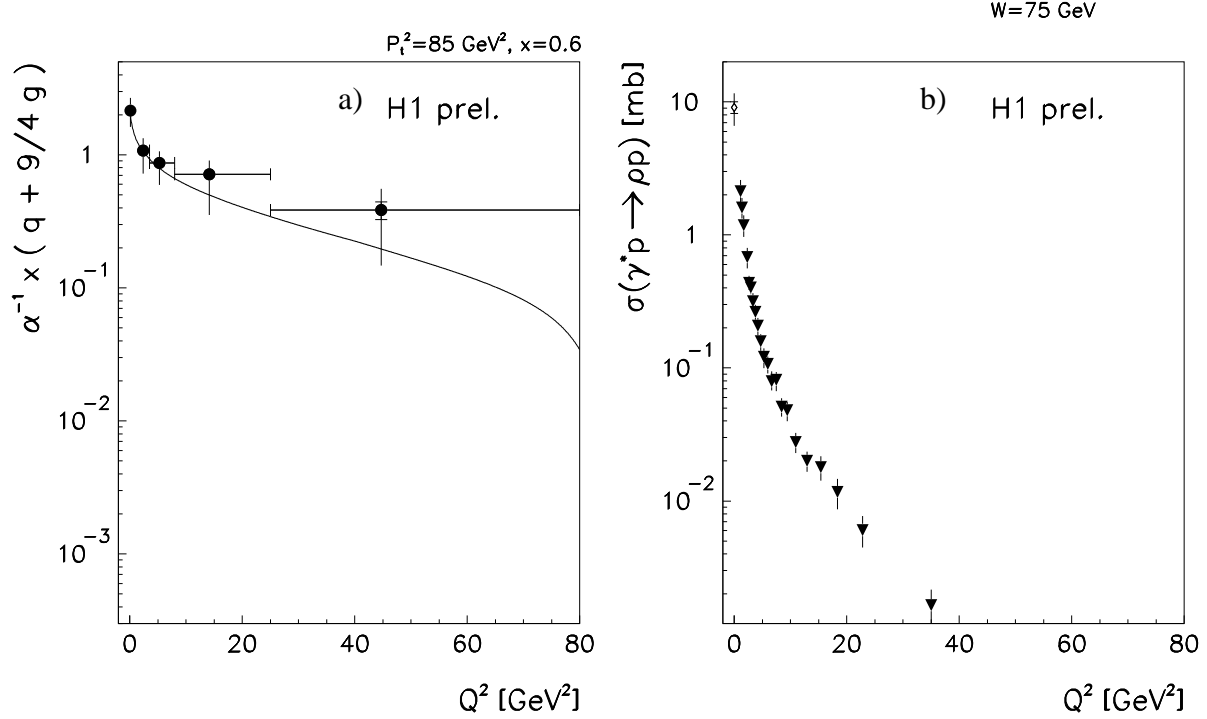


Figure 12: a) The effective parton distribution of virtual photons is shown as a function of the photon virtuality Q^2 for fixed parton fractional momentum $x = 0.6$ and scattered parton squared transverse momentum $p_t^2 = 85 \text{ GeV}^2$ (H1 experiment). The curve represents the SaS1d parameterization of the photon effective parton distribution. b) The ρ meson cross section is shown as a function of the photon virtuality Q^2 for the photon-proton center of mass energy $W = 75 \text{ GeV}$.

The proton tagged structure function is found to be larger than that of the neutron tagged data. The curves are predictions of model calculations inspired by Regge phenomenology (Fig. 15). In this picture, the proton data cannot be explained by π^0 exchange alone, since from the $\pi^0 p$ and $\pi^+ n$ isospin $1/2$ states one would expect the proton measurement to be a factor two below the neutron data. Instead, the proton data can be explained by an admixture of π^0 , Reggeon (f, ω) and Pomeron exchange. The neutron data can be explained by charged pion exchange alone and demonstrate the potential access to the pion structure function [31] in the new kinematic domain at small parton momenta around $x \sim 10^{-3}$.

Further information on the type of the interaction process comes from a new measurement of tagged baryons with the coincident formation of a large rapidity gap between the systems X and Y (Fig. 17) where Y may or may not be observed in the main detector (ZEUS collaboration [32]). In Fig. 18, the rate of events with a large rapidity gap is shown as a function of the baryon fractional energy $x_L \equiv z = E_{lb}/E_p$. For $x_L \rightarrow 1$, the tagged proton production (full circle) is dominated by diffractive processes. For $x_L \ll 1$, the minimum gap size chosen for the analysis implies that $M_Y > M_p$. In this kinematic region, the rate of events with a large rapidity gap is small and shows that diffraction is not the main mechanism for the production of the baryons.

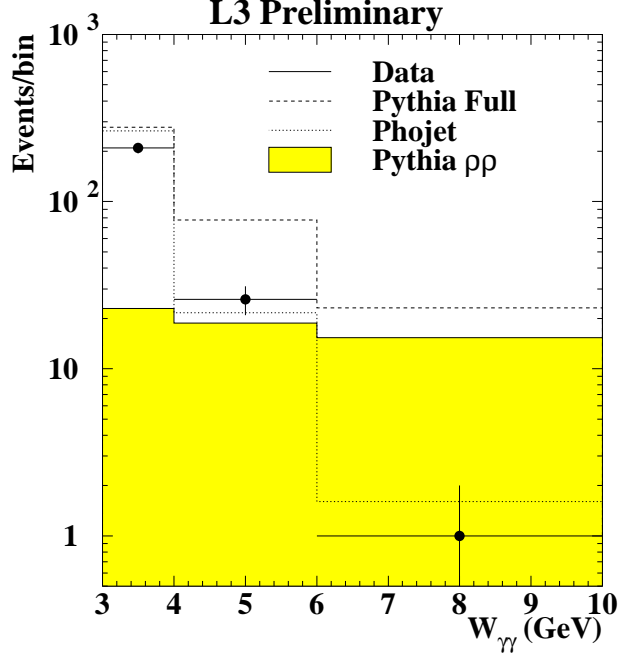


Figure 13: The number of events with exclusive four pion production from two-photon collisions in e^+e^- scattering is shown as a function of the photon–photon center of mass energy $W_{\gamma\gamma} \equiv \sqrt{s_{\gamma\gamma}}$ (L3 experiment). The data are compared with calculations of different Monte Carlo generators, showing the total four-pion production (histograms) and the exclusive production two ρ mesons (shaded histogram) separately.

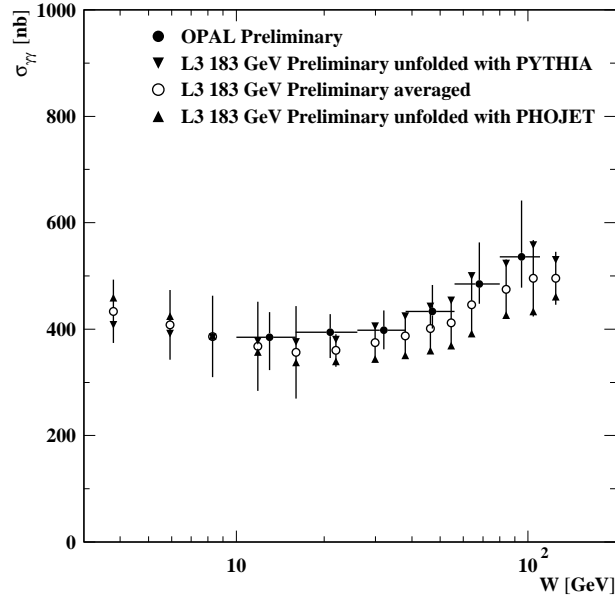


Figure 14: The total photon-photon cross section is shown as a function of the photon–photon center of mass energy $W_{\gamma\gamma} \equiv \sqrt{s_{\gamma\gamma}}$. The preliminary measurements of the L3 and OPAL experiments are compared using two different Monte Carlo generators for the detector corrections.

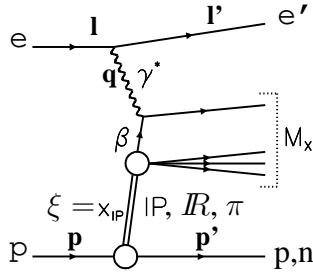


Figure 15: A Feynman diagram of deep inelastic electron–proton scattering with a tagged baryon is shown in the interpretation of colour singlet exchange.

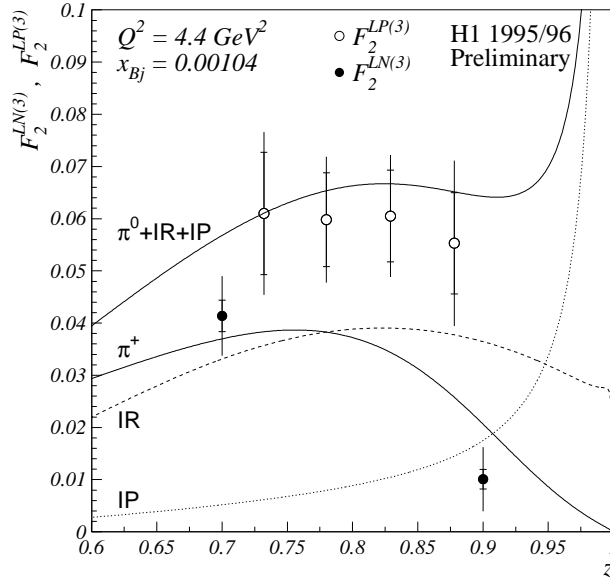


Figure 16: The ep structure functions $F_2^{LB(3)}$ with a tagged proton (open circle) or neutron (full circle) are shown as a function of the baryon fractional energy z at fixed photon virtuality $Q^2 = 4.4 \text{ GeV}^2$ and parton fractional momentum $x_{Bj} = 10^{-3}$ from H1 data. The curves represent the prediction of a Regge model.

2.2 The Partonic Structure of Diffractive Exchange

Evidence for diffractive scattering processes in ep interactions can be obtained from different methods:

- A** tagging of highly energetic protons in the proton spectrometers (Section 2.1),
- B** from analysis of rapidity regions which are free of hadronic activity (“rapidity gap”, Fig. 17),
or
- C** from the mass distribution of the hadronic final state which is observed in the main detector.

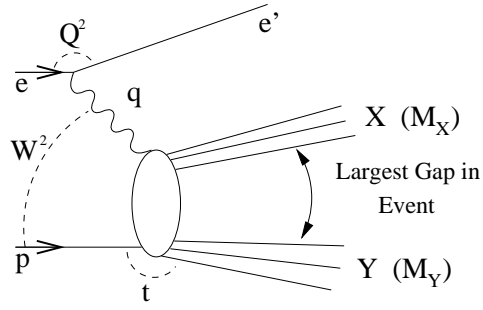


Figure 17: Feynman diagram of deep inelastic electron–proton scattering with a large rapidity gap.

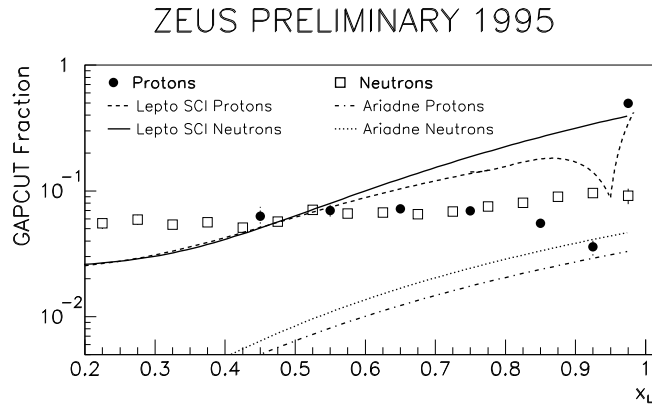


Figure 18: The rate of ep collisions with a tagged proton (full circle) or neutron (open square) with simultaneous formation of a rapidity gap is shown as a function of the baryon fractional energy x_L (ZEUS experiment). The curves show the predictions of different Monte Carlo generator calculations.

The ep Structure Function of Diffractive Exchange

The structure function $F_2^{D(4)}$ for diffractive exchange

$$\frac{d^4\sigma}{d\beta dQ^2 d\xi dt} = \frac{2\pi\alpha^2}{\beta Q^4} (1 + (1-y)^2) F_2^{D(4)}(\beta, Q^2, \xi, t) \quad (6)$$

has been measured by the ZEUS collaboration using the tagged proton method A [33] as a function of the following four variables:

1. the virtuality Q^2 of the exchanged photon.
2. the squared four-momentum transfer $|t| = (p - p')^2$ from the proton side,
3. the momentum fraction $\xi = (Q^2 + M_X^2)/(Q^2 + s_{\gamma^*p})$ ($\xi \equiv x_P$), with M_X being the mass of the diffractive system observed in the main detector, and
4. the fractional momentum $\beta = x_{Bj}/\xi$.

When interpreting this process in terms of the exchange of a colour singlet object (Fig. 15), ξ gives the fractional momentum that this object takes from the proton, and β is the fractional momentum of the quark involved in the electron-quark scattering process. Therefore, this deep inelastic scattering measurement gives access to the partonic structure of diffractive color singlet exchange and provides information on the corresponding t distribution of this process. A new measurement of the t distribution is shown in Fig. 19 (ZEUS collaboration [32]).

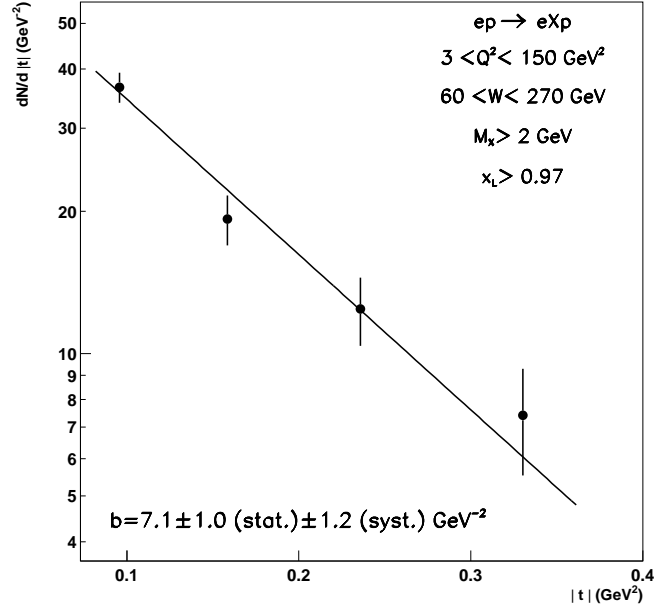


Figure 19: The distribution of the squared four-momentum transfer $|t|$ of diffractive ep processes is shown together with an exponential fit to the data (ZEUS experiment).

The methods B (Fig. 17) and C of measuring the deep inelastic scattering of diffractive exchange have to integrate over some t -range and can here take advantage of the knowledge of the t distribution of the proton tagged data. The two methods also do not include the detection of proton remnant particles at small masses M_Y of the dissociated proton system and integrate over a small range of this mass (typically 1-4 GeV). Since the acceptance of proton-tagged events is at the percent level, the statistics using methods B,C are much larger by far.

In Fig. 20, a new triple differential structure function measurements $F_2^{D(3)}$ of the ZEUS collaboration (method C [34]) are compared with previous measurements by the H1 collaboration (method B [35]). The data are shown in a small selection of the large phase space covered as a function of the fractional momentum ξ , which the colour singlet object takes from the proton, in two bins of the parton momentum observable β and the photon virtuality Q^2 .

At small ξ , they are consistent in these and surrounding phase space bins with a power law ξ^{-n} and therefore are compatible with factorization of the ξ dependence. The measured value by the ZEUS collaboration [34] is $n - 1 = 0.253 \pm 0.017^{+0.077}_{-0.023}$ and is compatible with the result of the H1 collaboration [35]. The measured value of n is slightly larger than the value expected for soft Pomeron exchange in Regge inspired models ($n - 1 \sim 0.1$).

The β and Q^2 dependence of $F_2^{D(3)}$ at fixed small value of ξ therefore gives the partonic structure of colour singlet exchange. The results of the two collaborations are consistent in

most of the 15 phase space regions commonly covered, for example in Fig. 20b, and call in a few of them for homework (Fig. 20a), especially in an understanding of slightly different kinematic regions covered in the squared momentum transfer t and the mass of the diffractive system M_Y .

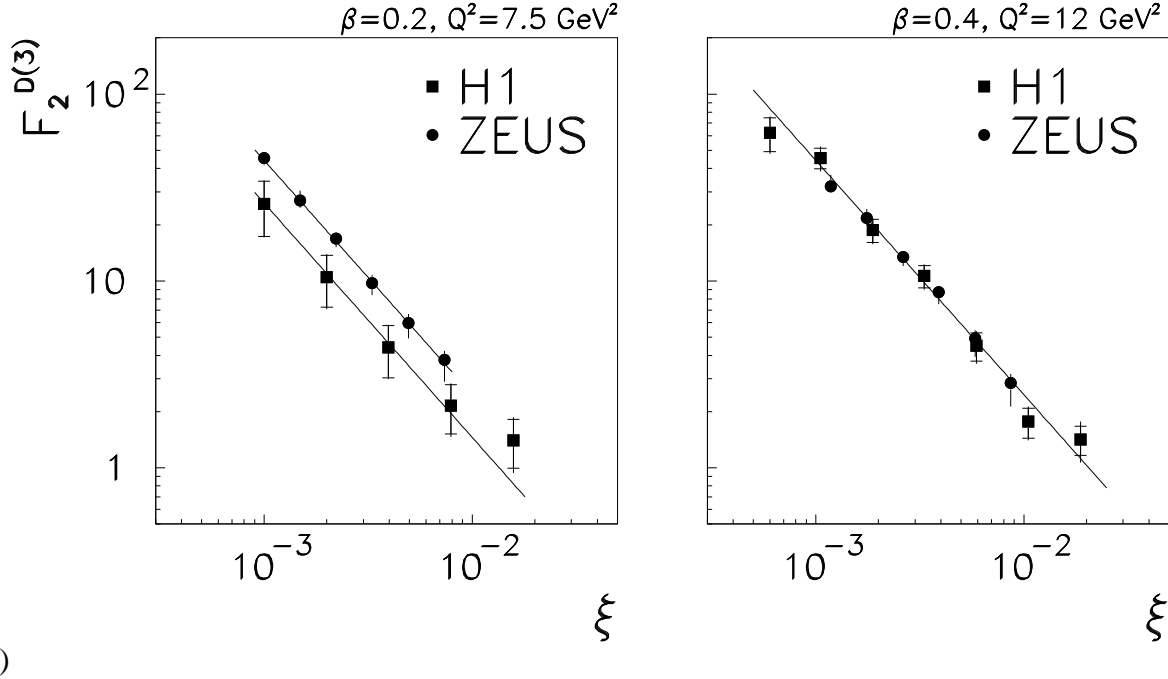


Figure 20: The ep structure function $F_2^{D(3)}$ of diffractive exchange is shown as a function of the fractional energy ξ of the exchanged object in two bins of the photon virtuality Q^2 and the parton fractional momentum β (H1 and ZEUS experiments). The curves have the functional form ξ^{-n} and serve the guidance of the eye.

In Fig. 21, the resolution scale Q^2 dependence of $F_2^{D(3)}$ of colour singlet exchange at large parton momenta $\beta = 0.4$ is shown. This measurement has been newly extended to large Q^2 up to 800 GeV^2 by the H1 collaboration [36]. The data are at relatively large values of $\xi = 0.02$ and can be described by a dominant diffractive exchange (Pomeron exchange) together with meson contributions (Reggeon exchange).

The Q^2 dependence of $F_2^{D(3)}$ is found to be consistent with flat which is very different from the structure function measurements of hadrons, e.g., the proton structure function (Fig. 5 [37]). It is also different from the Q^2 dependence of the photon structure function (Fig. 4). The different distributions can be understood from the QCD evolution equations: the probability f_q of finding a quark in the proton, color singlet exchange, or photon depends logarithmically on Q^2 :

$$\frac{df_q}{d \ln Q^2} = P_{qq} \otimes f_q + P_{qg} \otimes f_g + P_{q\gamma} \quad (7)$$

The $P_{ij} \otimes f_j$ denote the splitting functions convoluted with the parton densities. The first term $P_{qq} \otimes f_q$ represents the contribution of quarks after radiating a gluon. The second term $P_{qg} \otimes f_g$

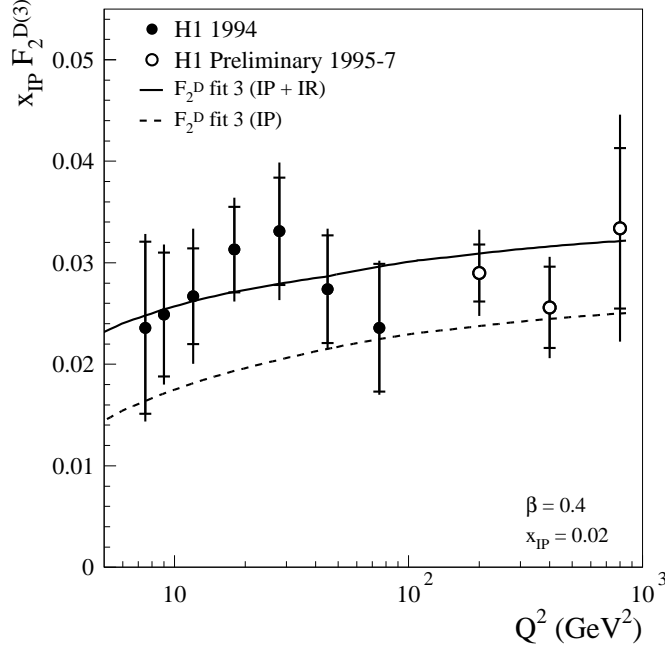


Figure 21: The structure function F_2 of the diffractive exchange is shown as a function of the virtuality Q^2 of the probing photon at the parton fractional momentum $\beta = 0.4$ and at the fractional momentum $\xi = x_{\text{IP}} = 0.02$ of the colour singlet object (H1 experiment). The curves are QCD fits to measurements below $Q^2 = 100 \text{ GeV}^2$.

gives the contributions of gluons that split into a quark–anti-quark pair. The third term $P_{q\gamma}$ adds the quarks resulting from the photon splitting into a quark–anti-quark pair (relevant for photon only).

The proton structure function falls at large $x = 0.4$ with increasing resolution scale Q^2 : the probability of finding a parton in the proton above the average valence quark momentum decreases with increasing resolving power Q^2 (first term of eq. (7)). The logarithmic increase of the photon structure function with Q^2 is caused by the third term of eq. (7) which is to first approximation independent of Q^2 .

The structure function of diffractive exchange differs from those of the proton and the photon: the flat shape makes it distinct from a quark dominated object. The large rate of diffractive exchange excludes an explanation by photon exchange. Instead, a large gluon density in the exchanged diffractive object can explain the observed Q^2 dependence of the structure function which is driven by the second term of eq. (7). Therefore the structure function measurement mainly probes the gluon splitting into a quark–anti-quark pair and reflects the structure of the strong interactions.

This partonic structure of colour singlet exchange has been quantified by extracting gluon and quark distributions from the diffractive data using the structure function measurements alone (H1 Collaboration [35]) or in combination with jet cross section measurements (ZEUS Collaboration [38]).

Different final state observables have been measured in diffractive ep scattering by the H1 and ZEUS Collaborations, e.g., thrust [39, 40], di-jet cross sections [41, 38], energy flow [42, 40], multiplicity [43], and charm production [44, 45]. A large fraction of the measurements have been compared to Monte Carlo generators which simulate diffractive ep scattering processes by the emission of colour singlet objects with the parton distributions as extracted from the fits to $F_2^{D(3)}$ mentioned above. Overall, the data are well described by such simulations which demonstrates a consistently working framework for understanding diffractive parton scattering processes in ep collisions. A deviation of this good description of the data may be seen in the photoproduction of di-jets which is discussed below in the comparison of the rates of diffractive processes at the HERA and Tevatron colliders.

Note that the picture of exchanging a colour singlet object with a partonic structure is not the only one to describe the data: interesting alternative approaches exist which need fewer parameters and describe certain aspects of the data well. Examples are electron scattering off a quark or a gluon of the proton with colour neutralization by the exchange of a second parton that cancels the colour charge, or models that predict the β dependence of $F_2^{D(3)}$, or the concept of fracture functions [46]. For reviews of the different approaches refer to, e.g., [47, 48].

Colour Singlet Exchange at the Tevatron

The methods used by the Tevatron experiments CDF and D0 to select diffractive scattering processes are detection of leading protons (method A) or measurement of rapidity gaps (method B). The observables used to analyse the diffractive exchange are di-jet formation and the production of W-bosons.

Both experiments have observed events involving the exchange of one or - as a new result - two colour singlet objects (Fig. 22a,c [49, 50]). In the latter process, the jets are produced centrally and in each beam direction a large rapidity gap or a tagged proton is observed. In Fig. 23, the shapes of transverse energy E_t^{jet} distributions of the leading jets in di-jet events are compared for single and double colour singlet exchange and non-diffractive data (CDF Collaboration). The E_t^{jet} range covered and the similarity of these distributions give several interesting observations:

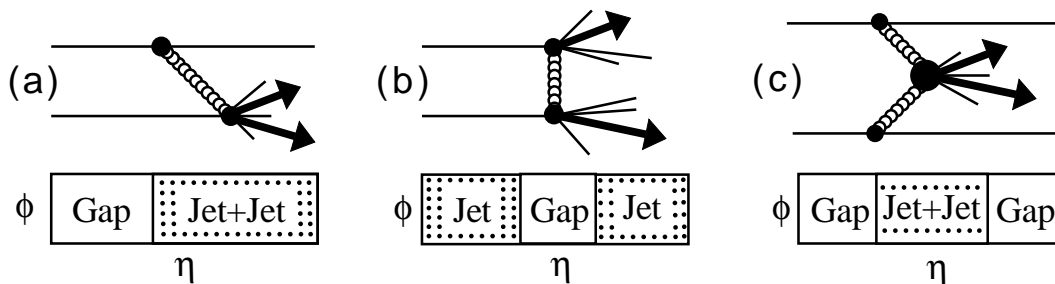


Figure 22: Di-jet production at the Tevatron with a) rapidity gap on one beam side, b) rapidity gap between the jets, or c) central jet production with two rapidity gaps.

The diffractive di-jet production results from the same type of parton-parton scattering processes as the non-diffractive data. In the latter case, the fractional momenta of the partons from

the proton are small $x \sim E_t^{jet}/\sqrt{s} \sim 10/1800$ and therefore likely to come from gluon–gluon scattering processes. In the diffractive case with the exchange of one or two colour singlet objects, the center-of-mass energy of the scattering process is much smaller than that of the $\bar{p}p$ beams since these objects carry only a fraction of the beam proton energy. Nevertheless, the jet transverse energy reaches out to $E_t^{jet} \sim 20$ GeV such that almost the full energy of these objects is involved in the hard parton–parton scattering process.

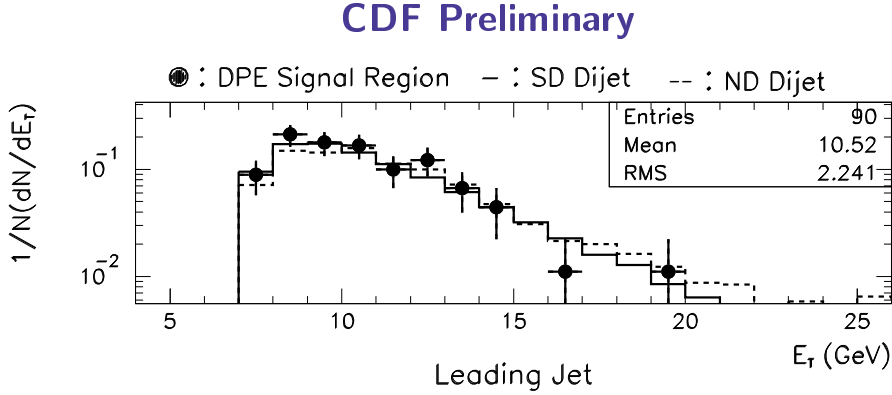


Figure 23: The shape of the transverse energy spectrum of the leading jet is shown from non-diffractive (dashed histogram), single diffractive (full histogram), and double diffractive (full circles) events in $\bar{p}p$ collisions (CDF experiment).

Both Tevatron experiments have observed events with a rapidity gap between two jets (Fig. 22b [49, 51]). In these events, the full energy of the exchanged object is involved in the jet production process and the object is probed at very large squared four-momentum transfer $|t|$ of the order of $(E_t^{jet})^2$. In Fig. 24, the rate of events with such a colour singlet exchange relative to non-diffractive events is shown from the D0 collaboration. The distribution of the size of the rapidity gap is shown to be within errors independent of the jet transverse energy (Fig. 24b,c). In Fig. 24a, the rate is given as a function of the jet transverse energy which has a tendency to rise with increasing E_t^{jet} .

The data are sufficiently precise to discriminate different models of colour singlet exchange: they exclude the exchange of a photon (dotted curves in Fig. 24) and a calculation using two hard gluons (“BFKL”, dashed curves [52]). The data can be consistently described by a model calculating the exchange of one energetic gluon with an additional parton to ensure colour neutrality (full curve [53]).

The CDF experiment has observed the production of W-bosons in diffractive scattering processes [54]. These events have essentially one lepton and missing transverse energy and can be interpreted as resulting from quark–anti-quark fusion. A comparison of the diffractive W-boson rate with that of the di-jet production is shown in Fig. 25 as a function of the relative gluon contribution in the colour singlet object and is expressed as a momentum sum rule. The gluon contribution is found to be large 0.7 ± 0.2 which is well compatible with previous (shown in the figure) and new fits of the ZEUS collaboration [38] (not shown) and previous results of the H1 collaboration [35].

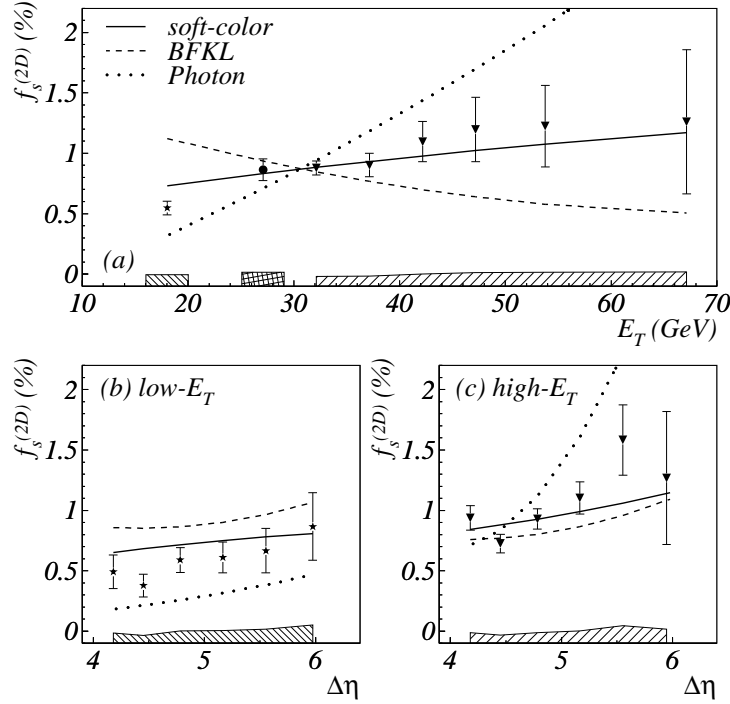


Figure 24: The rate of $\bar{p}p$ events with a rapidity gap between two jets is shown from preliminary D0 data: a) differentially in the transverse jet energy E_t^{jet} , and in b,c) as a function of the gap size $\Delta\eta$ for low and high values of E_t^{jet} . The curves represent the predictions of different model calculations.

Different Rates of Diffractive Processes at the HERA and Tevatron Colliders

While the large gluon component is consistently observed in diffractive processes at HERA and the Tevatron, the rate of such events is found to be largely different: at HERA, the rate of diffractive deep inelastic scattering events is of the order of 10%. In the phase space regions covered so far, the HERA final state data are overall consistently described when compared to calculations that use the parton distributions resulting from the diffractive structure function measurements. Using the same parton distributions for the Tevatron diffractive data, the predicted rate is much larger than the observed rate of the order of 1% [54, 55]. This discrepancy can, e.g., be expressed in terms of a momentum sum rule as shown in Fig. 25. The inconsistency is a puzzle which is under lively discussion.

Instructive measurements have been made, allowing the energy E_{ia} involved in the interaction to be measured relative to the total hadronic center-of-mass energy \sqrt{s} . In Fig. 26, rates of diffractive events are shown as a function of the ratio E_{ia}/\sqrt{s} .

For the Tevatron jet results [49, 50, 51], the jet transverse energy E_t^{jet} at the threshold has been used as a measure of E_{ia} (Fig. 26a-c). The rate of diffractive events appears to decrease as the total center-of-mass energy $\sqrt{s_{pp}}$ becomes large relative to the energy involved in the scattering process.

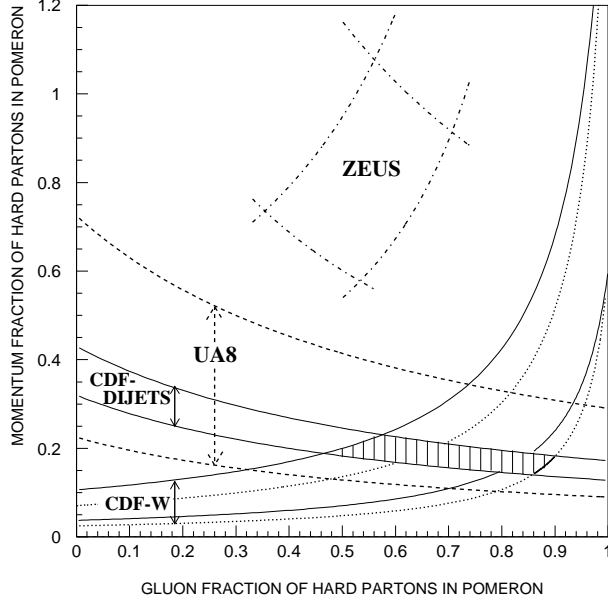


Figure 25: The total momentum fraction carried by the partons of the diffractive exchange object is shown as a function of the relative gluon contribution. The lower bands represent the region allowed from the measurements of diffractive di-jet production in $\bar{p}p$ collisions and W production respectively (CDF experiment). The bands in the upper half of the figure are a comparison of diffractive jet production with diffractive structure function measurements in ep collisions (ZEUS experiment).

Such dependence can, e.g., be explained by the increased potential of destroying the rapidity gap by beam remnant interactions which may be formulated in a reduced survival probability for the rapidity gap. Different other explanations have been suggested, key words are here absorption corrections, flux renormalization, or other means of factorization breaking [56, 57, 58].

For the HERA data, two measurements are discussed here: in the case of deep inelastic scattering data, the mass M_X of the diffractive system has been taken as a measure of E_{ia} . The data in Fig. 26d are consistent with being flat as a function of $M_X/\sqrt{s_{\gamma^*p}}$ [34] and show no indication of a decreasing survival probability.

In photoproduction of di-jets, the fractional momentum x of the parton from the photon is related to the ratio $E_t^{jet}/\sqrt{s_{\gamma p}}$. In Fig. 27, the di-jet cross section from diffractive scattering processes is shown as a function of x from H1 data [41]. At large $x \sim 1$, where the direct photon contribution dominates, the data are described by the calculations of the POMPYT generator [59] when using the parton distribution functions for the colour singlet exchange as extracted from the $F_2^{D(3)}$ measurements. However, at $x < 0.8$ the data are better described, if an overall reduction factor of $S = 0.6$ is applied to the calculation of the resolved photon–proton interactions. This observation hints for a reduced survival probability of the rapidity gap in resolved photon–proton processes. Owing to the presence of a proton and a photon remnant, these γp processes are similar to that of diffractive processes in $\bar{p}p$ collisions. In the future, more extended and precise measurements of the photoproduction of jets may help in the understanding of the different diffractive rates observed by the HERA and Tevatron experiments.

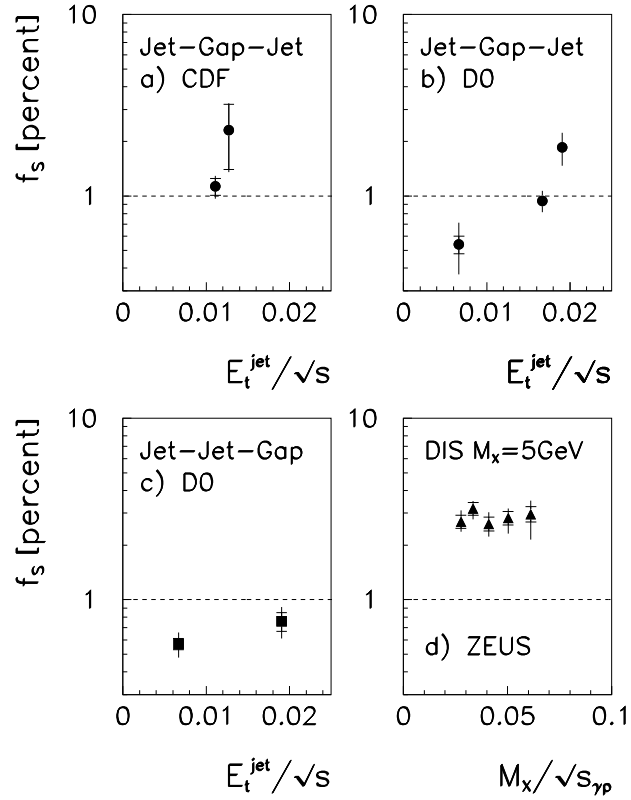


Figure 26: A comparison of the measured rates of diffractive interactions is shown as a function of the energy involved in the interaction relative to the total hadronic center of mass energy: a,b) rapidity gap signature between two jets of transverse energy above E_t^{jet} from $\bar{p}p$ collisions (CDF and D0 experiments), c) diffractive di-jet production in $\bar{p}p$ collisions (D0 data), and d) diffractive structure function in ep collisions where M_X denotes the mass of the diffractive system observed in the main detector (ZEUS experiment).

2.3 Vector Meson Production in ep Collisions

In elastic vector meson production from ep collisions, the full energy of the colour singlet object is involved in the scattering process (Fig. 28). Of special interest are processes with a hard scale such as

1. the mass M_V of a heavy vector meson,
2. the virtuality Q^2 of the photon in a deep inelastic scattering process, or
3. the squared four-momentum transfer t of the colour singlet exchange.

Such processes allow perturbative QCD calculations to be compared with the measurements and therefore give additional information on colour singlet exchange as well as on the proton and the vector meson [60].

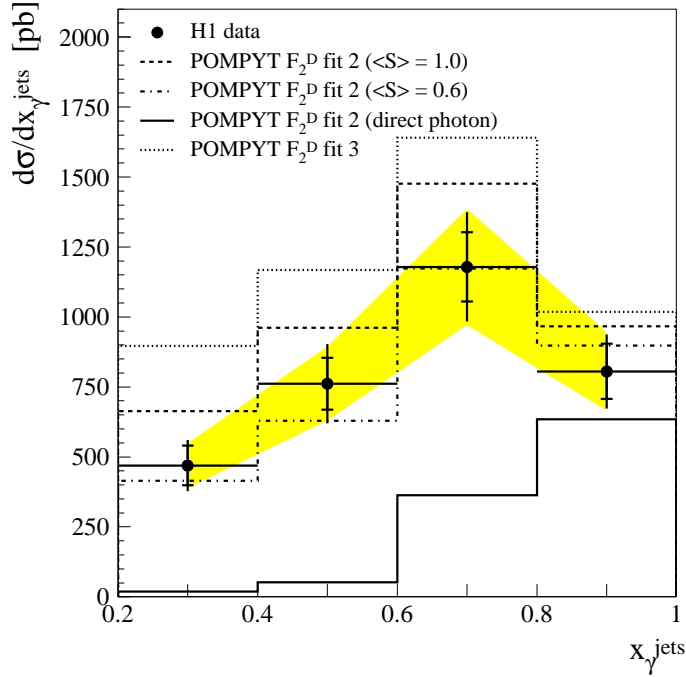


Figure 27: Photoproduction of di-jets in diffractive ep collisions is shown as a function of the fractional momentum x of the parton from the photon (H1 data). The dotted and dashed histograms show Monte Carlo generator calculations using two different parton distribution functions for the colour singlet exchange which were extracted from structure function measurements. The full histogram represents the contribution of direct photon–proton processes in diffractive interactions. In the dash-dotted histogram, a “rapidity gap survival factor” of $S = 0.6$ was applied to the calculation for the generated momenta of the partons from the photon below $x = 0.8$.

In this context, the following measurements of vector meson production in ep collisions at HERA are discussed here:

1. vector meson cross sections and their dependencies on the center-of-mass energy $\sqrt{s_{\gamma p}}$, the photon virtuality Q^2 , and the squared momentum transfer t , and
2. photoproduction of J/ψ mesons from proton and nuclear targets.

Measurements Related to the Gluon Distribution of the Proton

In Fig. 29, a compilation of the measurements of the total photoproduction cross section $\sigma_{\gamma p}$ and elastic vector meson cross sections $\sigma_{\gamma p}^V$ up to the production of Υ [61, 62] is shown as a function of the photon–proton center-of-mass energy $W \equiv \sqrt{s_{\gamma p}}$. The measured total cross section is at large center-of-mass energies compatible with a slowly rising distribution as

$$\sigma_{\gamma p} \sim s^\epsilon \quad (8)$$

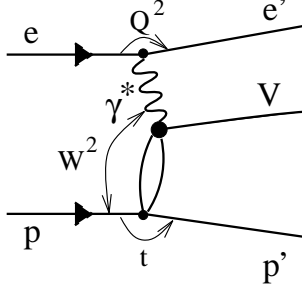


Figure 28: Feynman diagram of vector meson production in electron–proton scattering.

with $\epsilon \sim 0.095 \pm 0.002$ [29]. The optical theorem relates the total cross section to the imaginary part of the amplitude of forward elastic scattering. Therefore, elastic vector meson cross sections should rise with approximately twice the power:

$$\sigma_{\gamma p}^V \sim s^{2\epsilon}. \quad (9)$$

Photoproduction of light vector mesons (ρ , ω , ϕ) show an increase in the production that is compatible with this prediction. However, photoproduction of the heavy J/ψ mesons exhibit a stronger dependence on the center-of-mass energy with $\epsilon \sim 0.2$.

A steeper energy dependence is also observed for light vector meson production in deep inelastic scattering processes: in Fig. 30a, the energy dependence of new $\sigma_{\gamma p}^V$ measurements by the H1 and ZEUS Collaborations [24, 63, 64, 65] was again expressed in terms of the fit parameter ϵ using eq. (9) and is shown as a function of the scale. The scale was here chosen to be the sum of the photon virtuality and the vector meson squared mass $Q^2 + M_V^2$. The parameter ϵ is found to increase with increasing scale.

Such energy dependence is similar to that observed in inclusive deep inelastic scattering cross sections (Fig. 30b [68]). At fixed Q^2 and small parton momenta x_{Bj} , the total photon–proton cross section $\sigma_{\gamma^* p}$ is directly related to the large gluon density observed in the proton which gives rise to the $(x_{Bj})^{-\lambda}$ dependence of the proton structure function F_2 . Using the relation $x_{Bj}s_{\gamma^* p} \approx Q^2 = \text{const.}$ gives an energy dependence of the cross section as $\sigma_{\gamma^* p} \sim F_2 \sim (x_{Bj})^{-\lambda} \sim (s_{\gamma^* p})^\lambda$. The similar energy dependencies observed in vector meson production (Fig. 30a) and inclusive deep inelastic scattering processes (Fig. 30b) is suggestive of sensitivity of the vector meson data to the gluon distribution of the proton.

In Fig. 31, the longitudinal component of the ρ meson production cross section is shown as a function of x_{Bj} in four bins of Q^2 [63]. Similarly, the J/ψ production cross section is shown in Fig. 32 as a function of the photon–proton center-of-mass energy $W \equiv \sqrt{s_{\gamma^* p}}$ [65].

The measurements can be described by perturbative QCD calculations which use existing parameterizations of the gluon distributions in the proton (curves [66, 67]). The calculations use the square of the gluon density to account for the colour neutrality of the exchanged object (e.g. Fig. 33). Therefore, the comparisons of the data with the calculations give a highly sensitive measure of the gluons in the proton. A further component of the calculations is the mechanism for formation of the vector meson such that the comparisons to the data will give new information also on this part of the process.

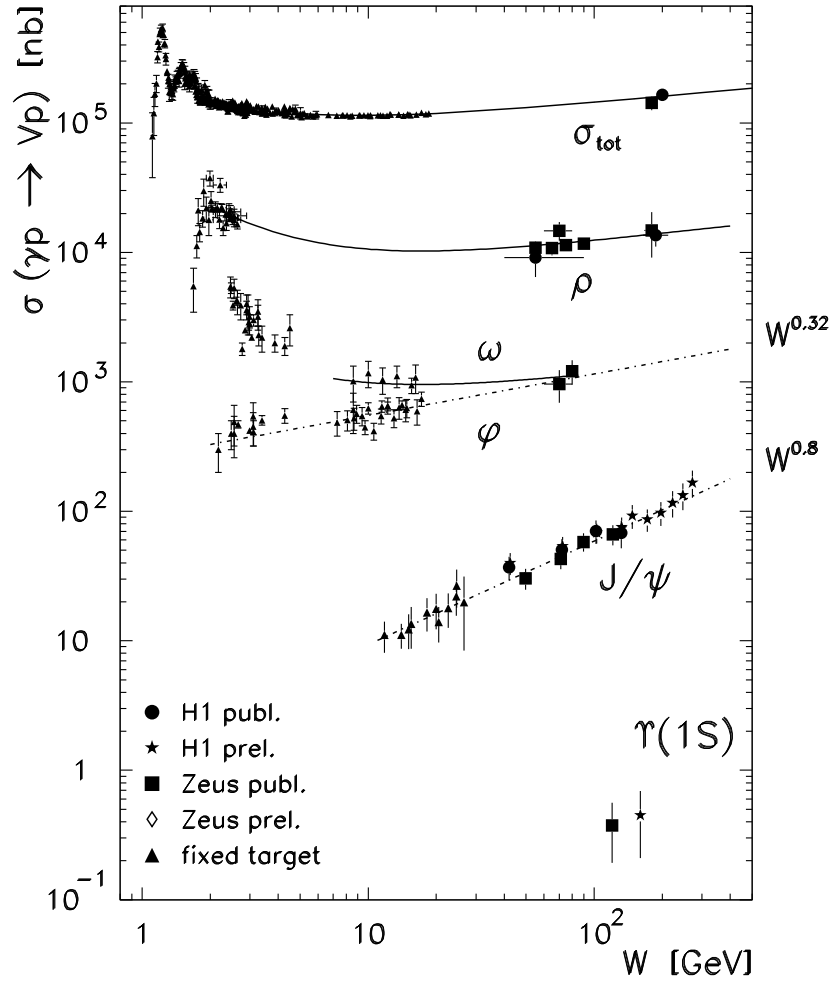


Figure 29: The photon-proton total cross section and vector meson cross sections from fixed target experiments and ep collisions at HERA are shown as a function of the photon-proton center of mass energy $W \equiv \sqrt{s_{\gamma p}}$. The full curves represent the predictions of a Regge model. The dashed curves are functions of the form $W^\delta \equiv (s_{\gamma p})^{2\epsilon}$ to guide the eye.

Measurements Related to Quark–Anti-Quark States

In elastic vector meson production, the squared momentum transfer t , which is exchanged between the vector meson and the proton, gives information on the size of the interaction region. Such t distributions can be fitted for small values of t using an exponential distribution $\exp(-bt)$.

In Fig. 34, a compilation of the fitted b parameters is shown for the HERA data for ρ , φ , and J/ψ meson production as a function of the scale (new measurements: [24, 63, 64, 65]). The scale has here again been chosen to be the sum of the photon virtuality Q^2 and the vector meson squared mass M_V^2 . With increasing scale, the data tend to approach a constant value of $b \sim 4 \text{ GeV}^{-2}$ which corresponds to the size of the proton. The size of the $q\bar{q}$ state is therefore small

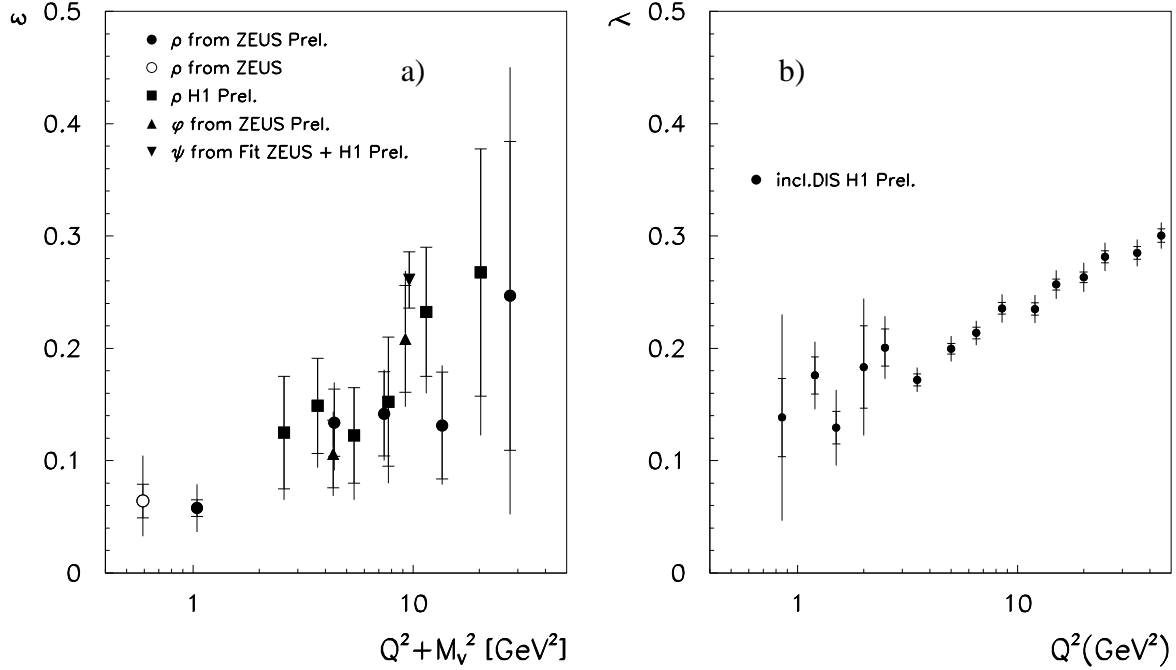


Figure 30: a) The energy dependence of vector meson cross sections $\sigma_{\gamma p}^V \sim (s_{\gamma^* p})^{2\epsilon}$ in ep collisions is shown as a function of the scale taken here to be the sum of the photon virtuality Q^2 and the vector meson squared mass M_V^2 (H1 and ZEUS experiments). b) The energy dependence of inclusive cross section measurements $\sigma_{\gamma^* p} \sim (s_{\gamma^* p})^\lambda$ is shown as a function of the photon virtuality Q^2 from H1 data.

compared to that of the proton and probes the proton at small distances.

The b parameter measured for the photoproduction of J/ψ mesons indicates the small size of the charm–anti-charm object in the interaction with the proton. Further information on this $c\bar{c}$ configuration results from nuclear dependencies of non-diffractive J/ψ meson production in comparison to that of protons [69]:

In Fig. 35, the shapes of proton–nucleus cross sections $pA \rightarrow pX$ [70] are shown as a function of the rapidity change Δy . Here Δy denotes the rapidity difference between the beam proton and the most energetic tagged proton. These distributions can be described by an exponential form $\exp(-\Delta y/\Delta y_0)$. The fitted slopes decrease as the nuclear mass increases, i.e., the protons are on average more decelerated with a heavier target.

It is interesting to compare the deceleration process of the protons with that of J/ψ mesons resulting from non-diffractive photoproduction off nuclei $\gamma A \rightarrow J/\psi X$. Here the rapidity difference between the photon and the J/ψ is used as a measure of the deceleration process (Fig. 35, data of the EMC [71], H1 [72], and ZEUS [73] experiments).

Also these distributions in the rapidity difference can be described by an exponential form. In contrast to the proton data, the slope of the J/ψ production does not decrease with increasing mass of the nucleus which implies that the iron target does not decelerate the $c\bar{c}$ object better than the proton target. The slight increase in the slope with A can be explained, according to Monte Carlo generator studies, by the different center-of-mass energies of the EMC and the HERA experiments.

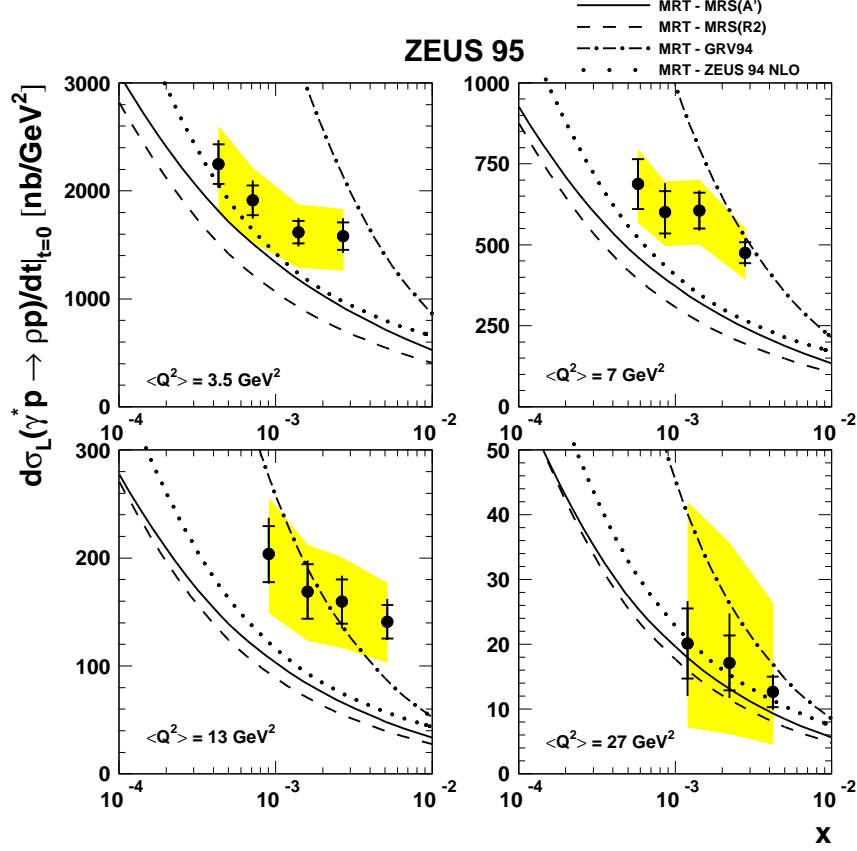


Figure 31: The longitudinal ρ meson cross section from deep inelastic ep scattering is shown as a function of the proton parton fractional momentum x_{Bj} in four bins of the photon virtuality Q^2 (ZEUS experiment). The curves represent the predictions of QCD calculations using different gluon distributions of the proton.

The absence of a nuclear deceleration effect for the J/ψ mesons may be interpreted as resulting from nuclear transparency. For a discussion of nuclear transparency effects refer, e.g., to [74]. In this interpretation, the colour charges of the small quark–anti-quark configuration are sufficiently screened to penetrate a nucleus without further interactions.

2.4 Summary 2: Colour Singlet Exchange

The HERA and Tevatron experiments have measured different observables that can be related to the parton distributions of diffractive exchange. Using structure function measurements in ep collisions, di-jet production in ep and $\bar{p}p$ scattering, and W-Boson production in $\bar{p}p$ collisions, they consistently find a large gluon component in this colour singlet state.

The overall rate of diffractive processes observed in ep and $\bar{p}p$ collisions, however, is found to be different and challenges explanation.

Measurements of elastic vector meson production involving a hard scale provide an alternative approach to understanding colour singlet exchange. Comparisons of the data with QCD

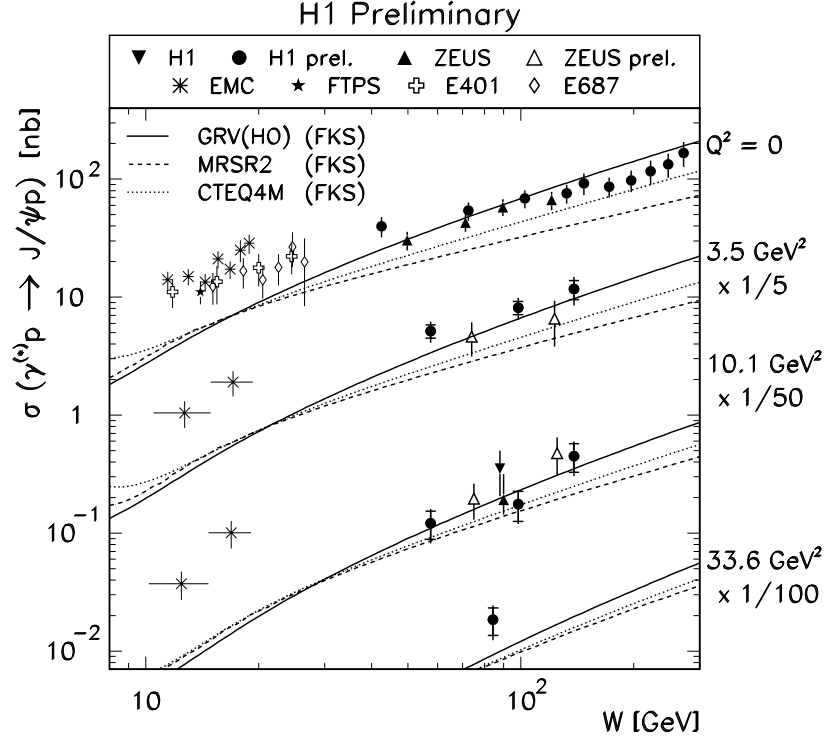


Figure 32: The J/ψ cross section from fixed target experiments and ep collisions at HERA is shown as a function of the photon-proton center of mass energy W in four bins of the photon virtuality Q^2 . The curves represent the predictions of QCD calculations using different gluon distributions of the proton.

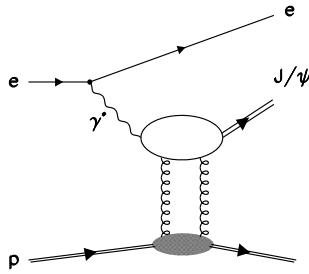


Figure 33: Feynman diagram of J/ψ meson production in electron–proton scattering with two-gluon exchange.

calculations that rely on two-gluon exchange give new information on the gluon distribution of the proton and on the vector meson states.

At sufficiently large scales, the spatial extension of the quark–anti-quark states appears to be small. Photoproduction of J/ψ mesons indicates that the $c\bar{c}$ state penetrates a nuclear environment essentially undisturbed.

Overall, diffractive physics is a very active field of research and is developing away from a soft interaction language to the understanding of a fundamental process of strong interactions within the framework of QCD.

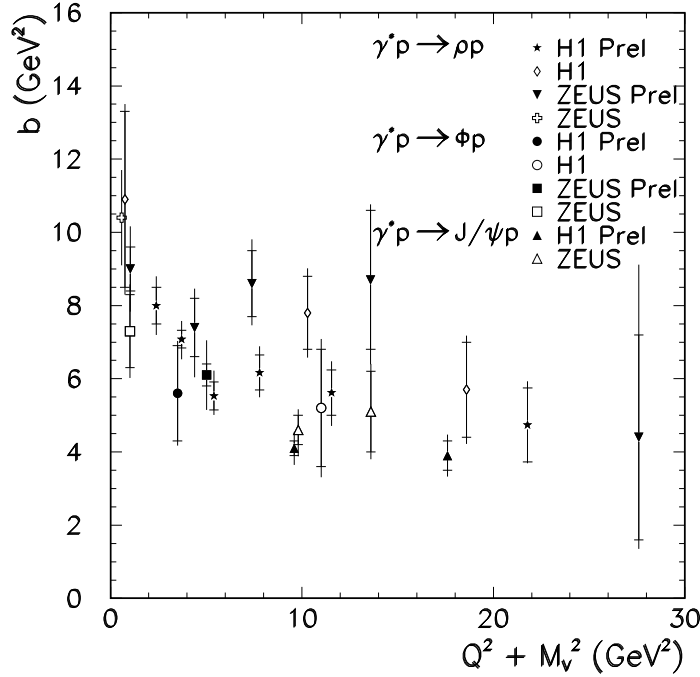


Figure 34: The fitted b parameter of the four-momentum transfer t distribution $\exp(-bt)$ is shown for the production of different vector mesons in ep collisions at HERA as a function of the scale which is here taken to be the sum of the photon virtuality Q^2 and the vector meson squared mass M_V^2 .

Acknowledgements

I wish to thank A. Astbury for providing a very positive conference atmosphere for the exchange of the new scientific results. I wish to thank for kind help in preparing the talk H. Abramowicz, M. Albrow, V. Andreev, K. Borras, A. Brandt, J. Dainton, T. Doyle, K. Freudenreich, C. Glasman, B. Heinemann, M. Kienzle, P. Newman, R. Nisius, G. Snow, and S. Söldner-Rembold. For careful reading of the manuscript and comments I wish to thank H. Abramowicz, M. Albrow, J. Dainton, M. Kienzle, P. Newman, G. Snow, and S. Söldner-Rembold. I am grateful to the Deutsche Forschungsgemeinschaft for the Heisenberg Fellowship.

References

- [1] M. Erdmann, *The Partonic Structure of the Photon*, Springer Tracts in Modern Physics, Heidelberg, Vol. 138 (1997)
- [2] L3 Collab., *Study of the Photon Structure Function F_2^γ at LEP*, paper 525 of the 29th Intern. Conf. on High-Energy Physics, Vancouver, Canada (1998)

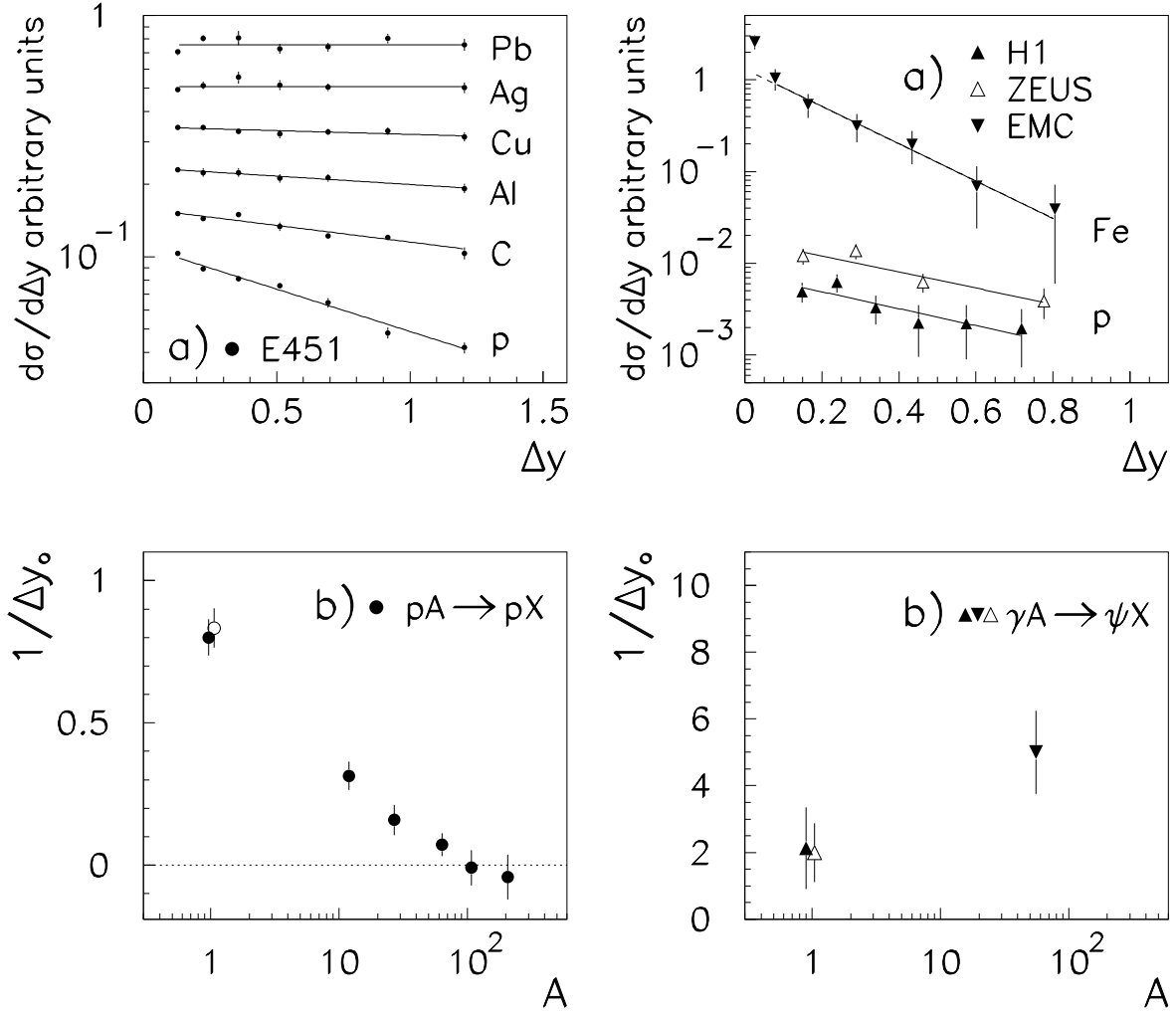


Figure 35: Left figures: a) shape of the rapidity change of beam protons in proton–nucleus interactions. The curves represent exponential fits to the data. b) The slopes $1/\Delta y_0$ of the fits in a) are shown as a function of the target mass A . Right figures: a) shape of the rapidity difference between the initial-state photon and the ψ meson observed in lepton–proton (triangle symbols pointing up) and lepton–iron interactions (triangle symbols pointing down). The curves represent exponential fits to the data. b) The slopes $1/\Delta y_0$ of the fits in c) are shown as a function of the target mass A .

- [3] R. Engel, *Z. Phys.* **C 66** (203) 1995,
R. Engel and J. Ranft, *Phys. Rev.* **D 54** (4244) 1996,
R. Engel et al., *Phys. Rev.* **D 46** (5192) 1992
- [4] TWOGAM 1.71, S. Nova et al., DELPHI note 90-35 (1990)
- [5] OPAL Collab., K. Ackerstaff, et al., *Phys. Lett.* **B 412** (225) 1997
- [6] H. Abramowicz, K. Charchula and A. Levy, *Phys. Lett.* **B 269** (458) 1991
- [7] M. Glück, E. Reya and A. Vogt, *Phys. Rev.* **D 46** (1973) 1992

- [8] G. A. Schuler and T. Sjöstrand, *Z. Phys. C* **68** (607) 1995
- [9] Compilation by R. Nisius (1998)
- [10] H1 Collab., C. Adloff, et al., *Eur. Phys. J. C* **1** (97) 1998
- [11] B.L. Combridge and C.J. Maxwell, *Nucl. Phys. B* **239** (429) 1984
- [12] ZEUS Collab., *High-Mass Di-Jet Cross Sections in Photoproduction at HERA*, paper 805 of the 29th Intern. Conf. on High-Energy Physics, Vancouver, Canada (1998)
- [13] M. Klasen, T. Kleinwort and G. Kramer, *Inclusive Jet Production in γp and $\gamma\gamma$ Processes: Direct and Resolved Photon Cross-Sections in Next-to-Leading Order QCD*, DESY-97-234 (1997), hep-ph - 9712256
- [14] L. E. Gordon and J. K. Storrow, ANL-HEP-PR-96-33, hep-ph-9607370 (1996)
- [15] L3 Collab., *Measurement of the Inclusive Charm Production in $\gamma\gamma$ Collisions at LEP with the L3 Detector*, paper 517 of the 29th Intern. Conf. on High-Energy Physics, Vancouver, Canada (1998)
- [16] M. Drees, M. Kramer, J. Zunft and P.M. Zerwas, *Phys. Lett. B* **306** (371) 1993
- [17] V. Andreev, private communications
- [18] H1 Collab., *Di-Jet Cross Sections in Photoproduction and Determination of the Gluon Density in the Photon*, paper 549 of the 29th Intern. Conf. on High-Energy Physics, Vancouver, Canada (1998)
- [19] OPAL Collab., G. Abbiendi, et al., *Di-Jet Production in Photon-Photon Collisions at $\sqrt{s_{ee}} = 161 \text{ GeV}$ and 172 GeV* , CERN-EP-98-113, subm. to *Eur. Phys. J. C* (1998)
- [20] T. Kleinwort and G. Kramer, *Nucl. Phys. B* **477** (3) 1996,
T. Kleinwort and G. Kramer, *Phys. Lett. B* **370** (141) 1996
- [21] T. Sjöstrand, CERN-TH-6488 (1992), *Comp. Phys. Commun.* **82** (74) 1994
- [22] H1 Collab., *Measurement of Di-jet Cross-Sections in Low Q^2 Deep-Inelastic Scattering Processes at HERA and the Extraction of an Effective Parton Density of the Virtual Photon*, paper 544 of the 29th Intern. Conf. on High-Energy Physics, Vancouver, Canada (1998)
- [23] H. Jung, *Comp. Phys. Commun.* **86** (147) 1995
- [24] H1 Collab., *Elastic Electroproduction of rho Mesons for $1 < Q^2 < 60 \text{ GeV}^2$ at HERA*, paper 564 of the 29th Intern. Conf. on High-Energy Physics, Vancouver, Canada (1998)
- [25] G. A. Schuler and T. Sjöstrand, *Phys. Lett. B* **376** (193) 1996
- [26] L3 Collab., *Cross section of hadron production in $\gamma\gamma$ collisions at LEP*, paper 519 of the 29th Intern. Conf. on High-Energy Physics, Vancouver, Canada (1998)

- [27] S. Söldner-Rembold, Proc. of the 29th Intern. Conf. on High-Energy Physics, Vancouver, Canada (1998), hep-ex 9810011
- [28] OPAL Collab., *Total Hadronic Cross-Section for Photon-Photon Interactions at LEP*, paper 199 of the 29th Intern. Conf. on High-Energy Physics, Vancouver, Canada (1998)
- [29] J.R. Cudell, K. Kang and S.K. Kim, *Phys. Lett. B* **395** (311) 1997, Review of Particle Physics, *Eur. Phys. J. C* **3** (1) 1998
- [30] H1 Collab., *Measurement of Leading Baryon Production at HERA and its Interpretation in terms of Colour Singlet Exchange*, paper 569 of the 29th Intern. Conf. on High-Energy Physics, Vancouver, Canada (1998)
- [31] B. Kopeliovich, B. Povh and I. Potashnikova, *Z. Phys. C* **73** (125) 1996
- [32] ZEUS Collab., *Leading Baryon Production in ep Scattering at HERA*, paper 789 of the 29th Intern. Conf. on High-Energy Physics, Vancouver, Canada (1998)
- [33] ZEUS Collab., J.Breitweg et al., *Eur. Phys. J. C* **1** (81) 1998
- [34] ZEUS Collab., J.Breitweg et al., *Measurement of the Diffractive Cross Section in Deep Inelastic Scattering using ZEUS 1994 Data*, DESY 98-084 (1998), acc. by *Eur. Phys. J. C*
- [35] H1 Collab., C. Adloff, et al., *Z. Phys. C* **76** (613) 1997
- [36] H1 Collab., *Measurement and Interpretation of the Diffractive Structure Function $F_2^{D(3)}$ at HERA*, paper 571 of the 29th Intern. Conf. on High-Energy Physics, Vancouver, Canada (1998)
- [37] H1 Collab., *Measurement of Inclusive Cross Sections for Neutral and Charged Current Interactions at High- Q^2* paper 533 of the 29th Intern. Conf. on High-Energy Physics, Vancouver, Canada (1998)
- [38] ZEUS Collab., J.Breitweg et al., *Diffractive Di-Jet Cross Sections in Photoproduction at HERA*, DESY 98-045, (1998) acc. by *Eur. Phys. J. C*
- [39] H1 Collab., C. Adloff et al., *Eur. Phys. J. C* **1** (495) 1998
- [40] ZEUS Collab., *Properties of hadronic final states in diffractive deep inelastic ep scattering at HERA*, paper 787 of the 29th Intern. Conf. on High-Energy Physics, Vancouver, Canada (1998)
- [41] H1 Collab., C. Adloff et al., subm. to *Eur. Phys. J. C*
- [42] H1 Collab., C. Adloff et al., *PLB* **428** (206) 1998
- [43] H1 Collab., C. Adloff et al., subm. to *Eur. Phys. J. C*
- [44] H1 Collab., *Production of $D^{*\pm}$ Mesons in Diffractive Interactions at HERA*, paper 558 of the 29th Intern. Conf. on High-Energy Physics, Vancouver, Canada (1998)

- [45] ZEUS Collab., *Open Charm Production in Diffractive Deep Inelastic Scattering at HERA*, paper 785 of the 29th Intern. Conf. on High-Energy Physics, Vancouver, Canada (1998)
- [46] D. de Florian and R. Sassot, *Fracture Functions for Diffractive and Leading Proton Deep Inelastic Scattering*, paper 986 of the 29th Intern. Conf. on High-Energy Physics, Vancouver, Canada (1998)
- [47] H. Abramowicz, J. Bartels, L. Frankfurt and H. Jung, *Diffractive Hard Scattering*, Proc. of the Workshop “Future physics at HERA”, eds. G. Ingelman, A. DeRoeck and R. Klanner, Vol.2, 635 (1996)
- [48] H. Jung, *Monte Carlo Implementations of Diffraction at HERA*, DESY-98-131, hep-ph - 9809374 (1998)
- [49] CDF Collab., *Diffractive Physics at CDF*, paper 928 of the 29th Intern. Conf. on High-Energy Physics, Vancouver, Canada (1998)
- [50] D0 Collab., *Hard Diffraction in $\bar{p}p$ Collisions at center-of-mass energies of 630 and 1800 GeV*, paper 469 of the 29th Intern. Conf. on High-Energy Physics, Vancouver, Canada (1998)
- [51] D0 Collab., *Probing Hard Color Singlet Exchange in $\bar{p}p$ Collision and 1800 GeV*, paper 467 of the 29th Intern. Conf. on High-Energy Physics, Vancouver, Canada (1998)
- [52] HERWIG 5.9 implementation of A.H. Mueller and W.K. Tang *Phys. Lett. B* **284** (123) 1992,
V. Del Duca and W.K. Tang *Phys. Lett. B* **312** (225) 1993
- [53] O.J.P. Eboli, E.M. Gregres and F. Halzen, MAD/PH-96-965 (1997)
- [54] CDF Collab., *Phys. Rev. Lett.* **78** (14) 1997
- [55] L. Alvero, J.C. Collins, J. Terron and J.J. Whitmore, *Diffractive Production of Jets and Weak Bosons, and Tests of Hard Scattering Factorization*, CTEQ-701-REV (1998), hep-ph - 9805268
- [56] E. Gotsman, E. Levin and U. Maor, *Energy Dependence of the Survival Probability of Large Rapidity Gaps*, hep-ph - 9804404 (1998)
- [57] K. Goulianos, *Pomeron Flux Renormalization: a Scaling Law in Diffraction*, hep-ph - 9806363 (1998)
- [58] S. Erhan and P.E. Schlein, *Phys. Lett. B* **427** (389) 1998
- [59] P. Bruni and G. Ingelman, *Diffractive Hard Scattering at ep and $\bar{p}p$ Colliders*, DESY-93-187 (1993), Proc. of the Europhysics Conference on High Energy Physics, Marseille, France, 595 (1993)
- [60] J.A. Crittenden, *Exclusive Production of Neutral Vector Mesons at the ep Collider HERA* Springer Tracts in Modern Physics, Heidelberg, Vol. 140 (1997)

- [61] ZEUS Collab., J. Breitweg et al., *Measurement of Elastic Υ Photoproduction at HERA*, DESY 98-089 (1998), acc. by *Phys. Lett. B*
- [62] H1 Collab., *Photoproduction of Υ Mesons at HERA*, paper 574 of the 29th Intern. Conf. on High-Energy Physics, Vancouver, Canada (1998)
- [63] ZEUS Collab., *Exclusive Electroproduction of ρ and J/ψ Mesons at HERA*, paper 792 of the 29th Intern. Conf. on High-Energy Physics, Vancouver, Canada (1998)
- [64] ZEUS Collab., *Exclusive Electroproduction of φ Mesons at HERA* paper 793 of the 29th Intern. Conf. on High-Energy Physics, Vancouver, Canada (1998)
- [65] H1 Collab., *Diffractional Charmonium Production in Deep Inelastic Scattering at HERA* paper 572 of the 29th Intern. Conf. on High-Energy Physics, Vancouver, Canada (1998)
- [66] A.D. Martin, M.G. Ryskin and T. Teubner, *Phys. Rev. D* **55** (4329) 1997
- [67] L. Frankfurt, W. Koepf and M. Strikman, *Phys. Rev. D* **57** (512) 1998
- [68] H1 Collab., *Precision Measurement of the Inclusive Deep Inelastic ep Scattering Cross Section at Low Q^2 at HERA*, paper 534 of the 29th Intern. Conf. on High-Energy Physics, Vancouver, Canada (1998)
- [69] M. Erdmann and A. Meyer, *Rapidity Change of p and J/ψ in Nuclear Environment*, paper 1072 of the 29th Intern. Conf. on High-Energy Physics, Vancouver, Canada (1998)
- [70] D.S. Barton et al., *Phys. Rev. D* **27** (2580) 1983
- [71] EMC Collaboration, J.J. Aubert et al., *Nucl. Phys. B* **213** (1) 1983
- [72] H1 Collaboration, S. Aid et al., *Nucl. Phys. B* **472** (3) 1996
- [73] ZEUS Collaboration, J. Breitweg et al., *Z. Phys. C* **76** (599) 1997
- [74] L.L. Frankfurt, G.A. Miller and M. Strikman, *Ann. Rev. Nucl. Part. Sci.* **45**, 501 (1994)